Modelling and simulation of plasma heating with ICRF waves in JET tokamak

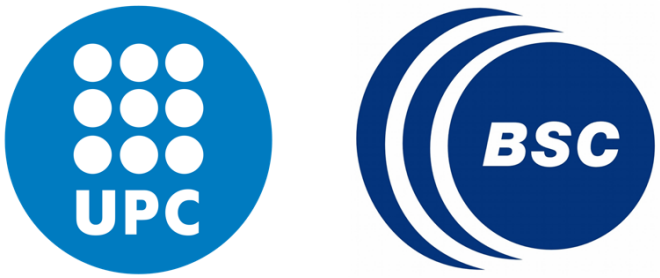

Eric Planas Parra

BACHELOR'S THESIS IN ENGINEERING PHYSICS

Supervisors
Dr. Dani Gallart
Prof. Mervi J. Mantsinen
Co-supervisor
Prof. Jordi José

Universitat Politècnica de Catalunya

ETSETB June 2020

Acknowledgements

I would like to express my sincere gratitude to those who have made possible the realization of this thesis and that have supported me during these months.

First of all, I would like to thank Prof. Mervi Mantsinen for giving me the opportunity to join the Fusion Group at Barcelona Supercomputing Center to perform my Undergraduate thesis. Besides, I also thank her for supervising my progress and for her advice. I am also very grateful to all the other members of the group, as I felt welcome since the very first day and they have been very supportive all this time.

Of course, this project would not have been possible without my supervisor Dr. Dani Gallart. I am deeply thankful for his patience and the amount of hours that he has dedicated to me, both at the office and when working from home. I barely had any knowledge on the field when I started this project, so I owe him everything I have learnt. He has been my guidance all along, and even in these challenging times due to the COVID-19 outbreak, he has been extremely supportive and comprehensive. I am also really thankful for all the long and fruitful conversations with him and for his invaluable advice, both at professional and personal levels.

I would also like to thank all the Engineering Physics program staff, specially my co-director Prof. Jordi José, who has helped me in everything I asked him for.

Finally, I am very grateful to my parents and the rest of my family and friends for their support and their trust in me, not only during the realization of this thesis, but during all these years at university.

Abstract

One of the challenges that magnetic confinement fusion faces is achieving extreme temperatures inside the reactors. Absorption of electromagnetic waves in the ion cyclotron range of frequencies (ICRF) has demonstrated efficient plasma heating in present-day tokamak experiments and it is one of the three auxiliary heating methods foreseen for the International Thermonuclear Experimental Reactor (ITER). Therefore, the study of different heating schemes using ICRF waves is of utmost interest to optimize the fusion performance.

The present thesis is focused in the computational assessment of plasma heating with ICRF waves and neutral beam injection (NBI) using the PION code. Strong emphasis is given to the physics behind these heating mechanisms and how they affect the fusion performance.

This project has been carried out in the context of the present deuterium (D) campaign that is being performed at the Joint European Torus (JET) experimental reactor in preparation for the next deuterium-tritium (D-T) campaign DTE2, which is planned to begin in 2021.

The results presented in this thesis consist of two parts. In the first part we model several D plasma discharges carried out at JET. The aim is to validate the current models used in PION and assess the role of different heating characteristics in the fusion yield in pure D plasmas. These experiments featured heating schemes based in minority populations of helium-3 (^{3}He) and hydrogen (H).

The second part of this project is focused on the extrapolation of a high performance plasma discharge to a 50%:50% D-T scenario. The study of D-T prediction is particularly relevant for the incoming campaign at JET and for ITER plasmas. A comparison of the heating characteristics with pure D plasmas is provided, and special attention is given to the resulting fusion yield in H and ^{3}He minority heating schemes in this scenario.

Table of contents

List of figures **vi**

List of tables **vii**

1 Introduction to the basic concepts of magnetic confinement fusion **1**

1.1 On the motivation for fusion power research 1
1.2 Nuclear fusion 2
1.3 Fusion reactors 3
1.3.1 Plasma confinement 3
1.3.2 Tokamaks and stellarators 4
1.3.3 Basic parameters of a tokamak 5
1.3.4 Goals and current issues 6
1.4 Plasma heating 7
1.5 Current experiments at JET and project goals 8

2 Physics of the ion cyclotron resonance frequency heating **10**

2.1 Maxwell equations in a plasma 10
2.2 The cold plasma model 12
2.3 Basic concepts on the wave propagation 13
2.3.1 Cutoffs and resonances 13
2.3.2 Accessibility 14
2.3.3 Wave polarization 14
2.4 Damping mechanisms 14
2.4.1 Ion cyclotron resonance damping 16
2.4.2 Direct electron damping 16
2.5 Heating schemes with ICRF waves 17
2.6 The distribution function 17
2.6.1 Collisional heating 18

2.6.2 Thermal and fast ions 18

3 Modelling of ICRF heating with the PION code 20
3.1 Introduction to the PION code 20
3.2 Brief description of the procedure 21
3.2.1 Modelling of the velocity distribution function. Fokker-Planck calculation 21
3.2.2 Modelling of power deposition 22
3.2.3 Modelling of the dielectric tensor 23

4 High performance D discharges at JET 25
4.1 Introduction 25
4.2 Analysis of H minority high performing discharges 26
4.2.1 Validation of the model 26
4.2.2 RF absorption in H minority discharges 28
4.2.3 Impact of channeling the wave power to D ions and non-thermal reactions 30
4.2.4 Impact of thermal reactions and bulk ion heating 32
4.3 ^{3}He heating in D plasmas 33
4.4 Chapter summary and discussion 35

5 Extrapolation of a high performance discharge to a D-T scenario 36
5.1 Introduction 36
5.2 H minority heating in a D-T scenario 37
5.3 Comparison of H and ^{3}He minority heating schemes in a D-T plasma . . . 39
5.3.1 RF absorption and collisional heating 41
5.3.2 Analysis of fusion performance in D-T plasmas 42
5.4 Chapter summary and discussion 44

6 Conclusions and final remarks 45

References 47

List of figures

1.1 Fusion cross-sections 3
1.2 Schematic views of a tokamak and a stellarator 5
1.3 Magnetic flux surfaces 6
1.4 Illustration of heating methods in fusion devices 7

2.1 Resonance positions 15
2.2 Banana orbits 19

4.1 Overview of the three modelled discharges 27
4.2 Experimental and simulated neutron yield of discharges 96482 and 96947 . 28
4.3 RF power absorption of discharges 96492 and 96947 29
4.4 Power absorption profiles for different H concentration for discharge 96947 30
4.5 Distribution functions of D in discharges 96482 and 96947 31
4.6 ICRF enhancement and collisionality of discharges 96482 and 96947 32
4.7 RF power absorption and collisionallity of discharges 96482 (H) and 94671 (^{3}He) 34

5.1 RF power absorption profiles of discharge 96482 in D and D-T scenarios . . 38
5.2 Collisional power profiles comparison between D and D-T scenarios 39
5.3 RF power absorption in a D-T scenario in a scan of minority concentration . 41
5.4 Collisional power in a D-T scenario in a scan of minority concentration . . 42
5.5 Neutron yield and distribution functions of H and ^{3}He schemes in a D-T plasma 43

List of tables

1.1 JET and ITER parameters 5

4.1 Maximum simulated neutron yield of discharge 96947 for different H concentrations 31

5.1 Comparison of the collisional power in the pure D and 50%:50% D-T scenarios 39
5.2 Reference values of minority, D and T densities for the scan in concentrations 40

Chapter 1

Introduction to the basic concepts of magnetic confinement fusion

The study of plasma physics and magnetic confinement fusion requires having basic knowledge of different fields (electromagnetism, fluid mechanics, statistical mechanics, engineering, etc.), so many concepts need to be introduced in order to understand the motivations, goals and results of this project. In this introductory chapter we attempt to summarize the basic ideas on magnetic confinement fusion and give an insight on the state of the art in order to put in context the project goals, while chapter 2 provides the fundamentals of the physics necessary to understand the results of this work.

1.1 On the motivation for fusion power research

Energy is a scarce resource. Nowadays, not only its demand has been dramatically increased, but also its current main sources such as fossil fuels are becoming more and more controversial due to climate change and their limited supply. This will inevitably lead at some point to the society collapse, so the world needs more than ever a new environmentally-friendly energy source capable of satisfying such demands to avoid the worst-case scenario.

While some alternatives to fossil fuels regarding the environmental impact have been presented (e.g. solar and wind energy), they appear not to be enough to cover the required power load. Moreover they are dependent on external issues such as the weather forecast. On the other side nuclear fission is capable of providing such power load, but it generates radioactive products which are dangerous for the environment and human health [17].

In this context fusion energy stands out as a solution to all these energy issues that could potentially be reached in a middle term. This is due to the fact that fusion power plants

would not produce radioactive residuals nor green-house gases, the fuel (hydrogen isotopes) is virtually unlimited and it has the potential to satisfy the energy demand.

Although the first electric plant powered by fusion energy is planned to be ready within 30 years from now, fusion research has made significant steps forward so far thanks to the current experimental reactors and all the international effort that is being put into this field.

1.2 Nuclear fusion

Nuclear fusion is a reaction in which two or more atomic nuclei combine and form a heavier nucleus. If this process occurs for nuclei with $Z < 26$, then it is exothermic, i.e. releases energy in form of kinetic energy. This is due to the fact that the mass of the resulting nucleus is smaller than the sum of the mass of the reactants. The missing mass is transformed into kinetic energy by following Einstein's formula $E = \Delta mc^2$. The mass defect is equal to the energy holding the nucleus together (i.e. the binding energy), so the reaction will be exothermic while the binding energy increases with the reaction.

This reaction takes place naturally at the stars' core, where the extreme pressure and temperature conditions make it possible for it to happen spontaneously. The energy release, in fact, prevents the star from collapsing under its own gravitational pressure. As it can be inferred, if fusion reactions are wanted to take place on Earth, the task of building a reactor is comparable with bringing the Sun to Earth [1]. In such conditions of temperature, the matter is in a plasma state [24]. Plasmas are, in essence, ionized gases that exhibit collective behaviours.

In this thesis, only the reactions between light elements will be considered as they are the ones that take place in the current experimental fusion reactors. In particular, the experiments that have been performed in the Joint European Torus (JET) reactor, which will be the subject of the present thesis, involve the hydrogen (H) isotopes, deuterium (D) and tritium (T). The D-D and D-T reactions are the most interesting ones to be remarked in this work, being:

$$D + D \rightarrow \begin{cases} T\ (1.01MeV) + p\ (3.02MeV) \\ {}^3He\ (0.82MeV) + n\ (2.45MeV) \end{cases} \tag{1.1}$$

$$D + T \rightarrow {}^4He\ (3.5MeV) + n\ (14.1MeV) \tag{1.2}$$

As stated before, these reactions occur in extreme conditions of temperature and pressure. The cross-section (σ) is a magnitude in surface units that is related to the probability of a

[1] https://fusionforenergy.europa.eu/

given fusion reaction to occur at a given temperature. In Fig. 1.1 the cross-sections of some reactions are displayed. It can be seen that σ_{DT} maximizes at lower energies as compared to other reactions. This is the reason why D-T plasmas are foreseen as the future fuel mixture in commercial reactors.

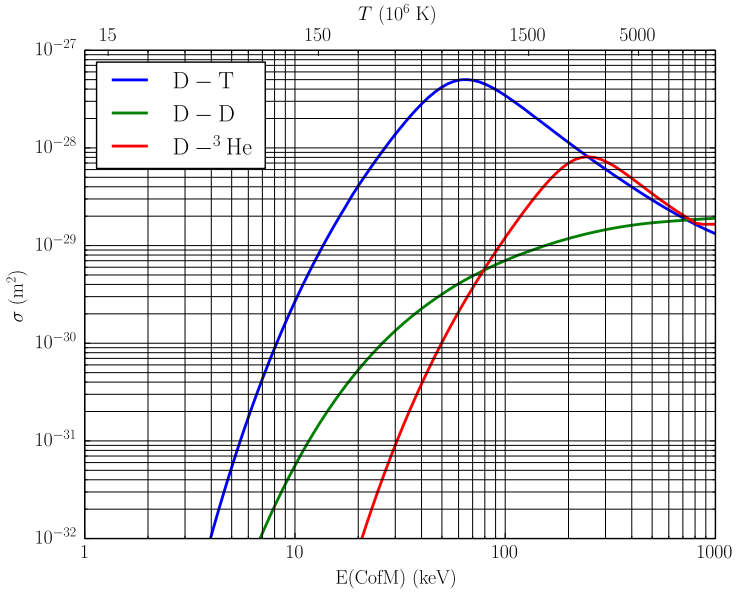

Fig. 1.1 *Fusion cross-sections for three different typical reactions in thermonuclear fusion as a function of the energy (and temperature) from the center of mass frame of reference (CofM).*

1.3 Fusion reactors

1.3.1 Plasma confinement

There are two main methods to confine a plasma and achieve fusion: inertial and magnetic confinement. In the present work the focus is on magnetic confinement. As plasma is composed by electrically charged particles, its confinement can be achieved by applying a magnetic field. The Lorentz force will act on ions and electrons which, assuming $\vec{B} = B_0\hat{k}$ and $\vec{E} = 0$, will describe a circular trajectory around the magnetic field lines (cyclotron motion). The solutions of the equations of motion are the following [7],

$$r_{\parallel} = v_{\parallel} t \hat{k} \tag{1.3}$$

$$r_{\perp} = \frac{v_{\perp}}{\omega_c} \cos(\omega_c t + \phi)\,\hat{i} + \frac{v_{\perp}}{\omega_c} \sin(\omega_c t + \phi)\,\hat{j}, \tag{1.4}$$

being $r_{\parallel}$ the parallel component of the motion to the magnetic field lines and $r_{\perp}$ the orthogonal component to the magnetic field lines. Here $v_{\parallel}$ corresponds to the parallel component of the velocity to the magnetic field, ϕ is an arbitrary phase angle and r_c and ω_c are the Larmor radius and cyclotron frequency, respectively, which are defined as $r_c = \frac{v_{\perp}}{\omega_c}$ and $\omega_c = \frac{ZeB_0}{Am}$.

1.3.2 Tokamaks and stellarators

Provided that the trajectories of electrically charged particles in magnetic fields are known, one can design a device to confine them effectively and prevent burning plasma from escaping. A possible solution to that consists of joining both sides of a solenoidal current and building a torus. This way, charged particles keep circling around endlessly. This is how the basis of the tokamak (from Russian "Toroidal chamber with magnetic coils") was born. However, the geometry of the resulting field, which is not uniform, prevents plasma from coming to an equilibrium force balance, causing it to expand through the walls and hence, producing the plasma loss [19]. This is overcome by inducing a toroidal current on the plasma itself, which produces a poloidal magnetic field that adds to the toroidal field created by the external coils. The field lines then describe helical paths around the torus, as shown in Fig. 1.2. The resulting magnetic field is able to avoid the outward radial particle drift and it provides a solution to reach an equilibrium force balance.

Tokamak plasmas, nevertheless, are subject to large instabilities as their stability depends on the current of the plasma itself. The stellarator was conceived as another solution to the plasma confinement in order to avoid them. This device, unlike tokamaks, is not axially symmetric and has a more complex shape (see Fig. 1.2), and the helical form of the magnetic field is achieved by currents in external windings rather than by toroidal currents. This is what entails such a complex geometry. Stellarators have demonstrated to prevent many plasma instabilities since the confinement does not depend on the plasma current. Nevertheless, tokamak research is more advanced and is the configuration used in most of fusion reactor design studies.

This thesis is focused on the experiments carried out at the largest currently operating tokamak, the Joint European Torus (JET), which is located in Culham, United Kingdom. At the same time, the International Thermonuclear Experimental Reactor (ITER) is currently under construction in Cadarache (France). It will be the largest experimental tokamak that has been ever built and it is the result of a large international project to bring fusion closer to reality. In this context, JET is now performing experiments in preparation for the future ITER operation. The next step is expected to be the construction of the Demonstration Power Plant (DEMO), which will be the first fusion-powered reactor to produce commercial energy.

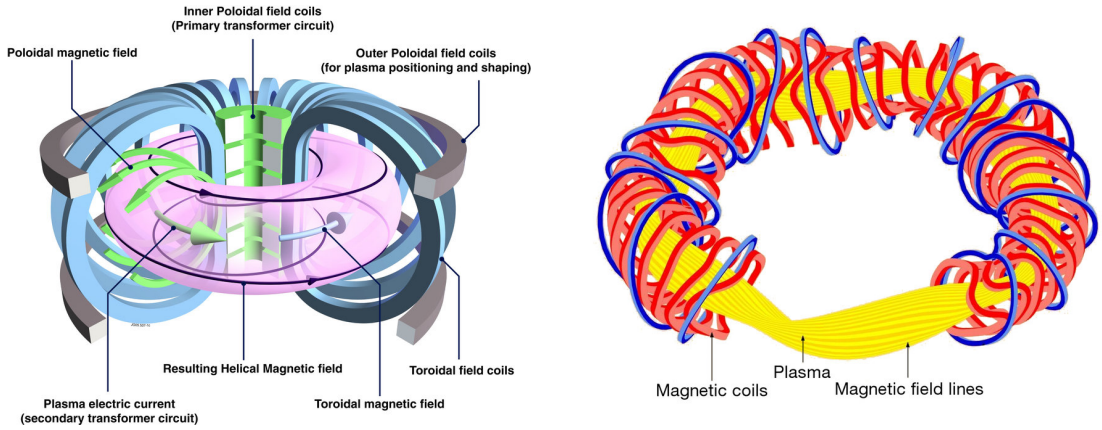

Fig. 1.2 *Schematic view of a tokamak (left) and a stellarator configuration (right), courtesy of EUROfusion and Max-Planck Institut für Plasmaphysik*

1.3.3 Basic parameters of a tokamak

Table 1.1 *JET and ITER parameters (courtesy of EUROfusion)*

Parameter	JET	ITER
Major radius R_0 (m)	2.96	6.2
Minor radius r (m)	1.25-2.10	2
Toroidal magnetic field B_T (T)	3.45	5.3
Toroidal plasma current I_p (MA)	4.8	15
Safety factor q_0	1.0	1.0
Safety factor q_{95}	5.0	3.5
Elongation κ	1.68	1.7
Triangularity δ	0.4	0.33
Plasma volume (m^3)	100	831
Fusion power (MW)	16	400-500

Tokamaks are characterized by a series of geometrical and plasma parameters. In Table 1.1 the design parameters of JET and ITER tokamaks are shown. The major radius R_0 corresponds to the distance between the center of the torus and the center of the poloidal section, while the minor radius r stands for the distance between the center of the poloidal section and the plasma surface. Actually, the poloidal section is not circular, but D-shaped. Elongation and triangularity are parameters related to such D-shape and refer to the plasma geometry inside the vacuum vessel.

The safety factor q of a tokamak is related with the magnetohydrodynamic (MHD) stability of the plasma. If $q \leq 2$ at the edge of the plasma, then the plasma is magnetohy-

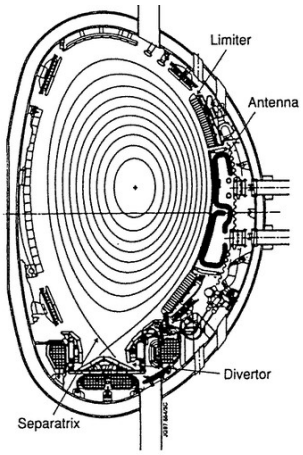

Fig. 1.3 [1] *Poloidal cross section of JET tokamak showing an schematic of the magnetic flux surfaces configuration, where their geometry forming a nested set is appreciated.*

drodynamically unstable. In Table 1.1 the q_0 and q_{95} factors refer to the safety factor at the plasma center and at the edge, respectively. In this section it is worth mentioning that the magnetic equilibrium, which has a strong impact on q, is given by the Grad-Shafranov equation [19], which is one of the most important equations in MHD of confined plasmas. With this equation the geometry of the magnetic flux surfaces (defined as $\vec{B} \cdot \hat{n}|_S = 0$, that is the surfaces where the magnetic field lines lie) can be found. The typical shape of the flux surfaces in a tokamak is shown in Fig. 1.3, and as they form a nested set, they can be labeled depending on the plasma volume that they enclose.

1.3.4 Goals and current issues

The goal of a fusion reactor is to achieve $Q > 1$, being Q the ratio of input power in the plasma to output fusion power. In particular, the goal of ITER is to achieve $Q = 10$. There exists an "ideal" condition, called the ignition condition, in which plasma would reach a self sustained state of continuous burning without any applied heating. This would lead to $Q \to \infty$, which means that the input power is equal to zero. The ignition condition is reached when the thermonuclear triple product $n_e \tau_E T$ surpasses a certain threshold, being n_e the electron density, τ_E the energy confinement time and T the temperature of the plasma. For the case of 50%:50% D-T mixtures, the ignition requirement is [24]

$$n_e \tau_E T > 3 \cdot 10^{21}\ m^{-3} keV s. \tag{1.5}$$

This means that T must be around 15 keV, τ_E about 2 s and n_e of 10^{20} m^{-3}. Beyond this threshold, the power of the $\alpha-$particles (i.e. ^{4}He particles) produced by fusion processes

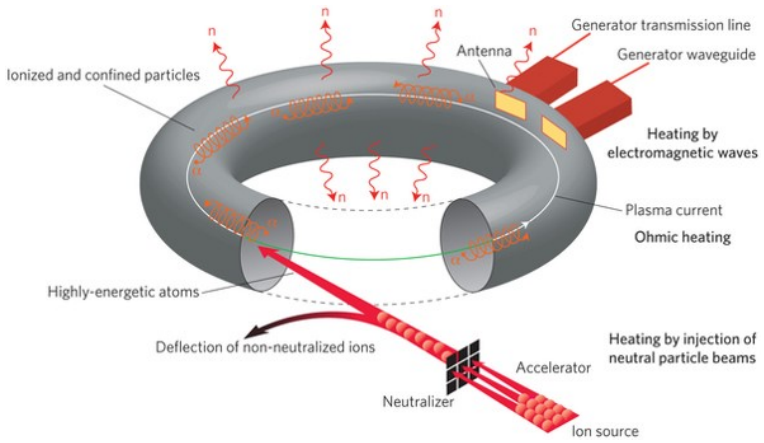

Fig. 1.4 *Schematic of the three main heating methods in current fusion devices.*

(Eq. 1.2) is enough to keep the plasma temperature, so no input power is needed. In the context of achieving plasma ignition, the main topics that are currently being addressed in fusion research are the following [7]: (1) macroscopic equilibrium and MHD stability, (2) transport phenomena, (3) heating and current drive, (4) alpha particle plasma physics and (5) fusion technology issues. This thesis addresses one of them: plasma heating.

1.4 Plasma heating

As seen in section 1.3.4, the required temperatures to reach plasma ignition are extremely high. For instance, the temperature required for reaching ignition in 50%:50% D-T plasmas is around 15 keV ($\sim$ 100 million °C). To reach this temperature, firstly the plasma must be heated until it reaches $5-7$ keV. During this transient regime the α power is negligible and the heating power must overcome the losses due to thermal conduction and Bremsstrahlung radiation [7]. Under proper confinement conditions, when plasma reaches $5-7$ keV the α power begins to dominate, heating it until the ignition temperature.

There exist several heating methods to make the plasma reach the desired temperature, depicted in Fig. 1.4. The toroidal current in a tokamak produces ohmic heating. This heating method can make plasma reach temperatures of about 3 keV. The plasma resistivity decays with temperature following the Spitzer resistivity [4]

$$\eta = \frac{\pi Z e^2 m_e^{1/2} \ln\Lambda}{\left(4\pi\varepsilon_o\right)^2 \left(k_B T\right)^{3/2}}, \tag{1.6}$$

where $\ln\Lambda$ stands for the Coulomb logarithm. At this point ohmic heating becomes inefficient. Therefore, when reaching these temperatures, alternative heating methods are needed.

One option is the neutral beam injection (NBI), where a beam of neutral particles is injected in the plasma. These particles can penetrate into the plasma since their trajectories are not initially affected by the magnetic field. Following the Beer-Lambert equation [7], they are ionized throughout their trajectory so that they become confined by the magnetic field. These particles have also a higher energy than the bulk particles, so when they are slowed-down by Coulomb collisions, they raise the bulk temperature of the plasma.

The other main option is the radio-frequency heating (RF heating). Here the energy of electromagnetic waves launched by antennas located inside the vacuum vessel is damped by ions and electrons and therefore, increasing the plasma temperature. RF heating can work in several regimes depending on the frequency used in the antennas. The two main regimes are the ion cyclotron resonance heating (ICRH) and the electron cyclotron resonance heating (ECRH) depending on whether ions or electrons are heated, respectively. Other regimes are used for different purposes. For instance, the lower-hybrid regime is used to drive non-inductive currents in the plasma (LHCD). The ICRH method is the central topic in which this thesis is focused. All the physics that concern this approach are discussed in detail in chapter 2.

1.5 Current experiments at JET and project goals

The present thesis is strongly related with the experiments carried out at JET tokamak so far, so it is important to put them in context in order to understand the relevance of this work.

In JET, several campaigns are being performed with different plasma mixtures before the D-T campaign (DTE2). These campaigns test the D majority and T majority which focus in three particular aspects of utmost relevance for the successful completion of DTE2 [11]: (1) What is going to be the impact of the isotope effect? (2) How can we assess the alpha generation and confinement? (3) How can we maximise the number of fusion reactions? A brief description for each of these questions is given in the following.

1. It has been found out that heat, particle and momentum confinement depend upon the average atomic mass (A) of the plasma and, therefore, it is expected that with higher presence of T (A = 3) within the plasma the confinement improves. This is the reason why separate campaigns with D majority (A = 2) and T majority (A = 3) are being performed. These experiments will allow to interpolate the confinement for a D-T plasma (A = 2.5).

2. D-T fusion reactions produce α-particles at an average energy of 3.5 MeV (see Eq. 1.2). These ions need to be confined in order to produce a self-sustained plasma, i.e. to

keep its high temperature. The ignition concept completely revolves around confining the alphas as explained in section 1.3.4. Therefore, schemes are being developed and tested so as to be able to properly diagnose the presence and impact of the alphas.

3. Maximising the number of fusion reactions is probably the main goal of these campaigns. In particular, $5 \cdot 10^{16}$ n/s needs to be showed for 5 seconds (D-D reactions) in order to achieve the goal of 15 MW of fusion power in D-T predictions. Plasma heating has a strong impact on the plasma performance. For this reason, several heating schemes are being addressed and assessed in order to understand not only the physics involved but also how these schemes could potentially be optimised.

This work tackles the third point (3) with two objectives. First, to validate the PION code (see chapter 3) against recent experimental data from the present JET campaigns, i.e., show that the code is capable of reproducing the heating related physics of the experiments. The goal is to study the heating aspects associated with the main heating schemes involved in these campaigns and its impact on the fusion rate (chapter 4). Second, once the code is validated a prediction for D-T plasmas will be performed (chapter 5) where the expected plasma performance will be tackled.

Therefore, this work will give an overview of the present plasmas from the heating point of view. The aim is to understand the physics involved in the different heating schemes with the final goal of studying their prediction to a D-T plasma.

Chapter 2

Physics of the ion cyclotron resonance frequency heating

In this chapter all the physics and formalisms about ICRH are discussed in detail. In particular, the Maxwell equations are solved applying the cold plasma model in order to see how electromagnetic waves in the ion cyclotron range of frequencies (ICRF waves) propagate into the plasma i.e. the dispersion relation is found. Besides, a discussion on some of the most important concepts related to ICRH is also provided, including the main wave damping mechanisms, the main strategies that are used to tackle ion energy absorption and the interaction between fast ICRH-driven ions and background plasma.

2.1 Maxwell equations in a plasma

The propagation of a wave in a plasma is not a trivial issue. Plasma is in fact too complex to be considered a material medium with permittivity ε as for dielectric materials. The key idea is to consider that a plasma consists in a set of charged particles immersed in vacuum, and that the response to an electric field excitation falls in the current density $\vec{J}$ and not in the polarization $\vec{P}$ or the magnetization $\vec{M}$ [7]. Hence, this section aims to understand the wave propagation by calculating the wave equation in a plasma medium under this premise.

We start from Maxwell equations:

$$\nabla \cdot \vec{E} = \rho/\varepsilon_0 \tag{2.1a}$$

$$\nabla \times \vec{E} = -\partial \vec{B}/\partial t \tag{2.1b}$$

$$\nabla \times \vec{B} = \mu_0 \vec{J} + \frac{1}{c^2}\frac{\partial \vec{E}}{\partial t} \tag{2.1c}$$

$$\nabla \cdot \vec{B} = 0. \tag{2.1d}$$

Assuming small perturbations from equilibrium, all quantities can be expanded as $Q(\vec{r},t) = Q_0 + \tilde{Q}_1(\vec{r},t)$, being $Q_0 \gg \tilde{Q}_1$ and Q_0 an homogeneous solution. Then, Fourier analysis can be used with $\tilde{Q}_1(\vec{r},t)$ so that it is written as

$$\tilde{Q}_1(\vec{r},t) = Q_1 \exp(-i\omega t + i\vec{k}\cdot\vec{r}). \tag{2.2}$$

The derivatives in Maxwell equations then become $\nabla \to i\vec{k}$ and $\partial/\partial t \to -i\omega$. On the other hand, applying the curl to Faraday's law (2.1b) and then plugging Eq. (2.1c) we get

$$\nabla \times \nabla \times \vec{E}_1 = -\mu_0 \frac{\partial \vec{J}_1}{\partial t} - \frac{1}{c^2}\frac{\partial^2 \vec{E}_1}{\partial t^2}, \tag{2.3}$$

which, applying Fourier analysis, leads to

$$\vec{k} \times \vec{k} \times \vec{E}_1 = -i\omega\mu_0 \vec{J}_1 - \frac{\omega^2}{c^2}\vec{E}_1. \tag{2.4}$$

Using the dimensionless index $\vec{n} = \frac{c}{\omega}\vec{k}$ and considering that $\vec{J}_1 = \bar{\sigma}\cdot\vec{E}_1$, where $\bar{\sigma}$ is the conductivity tensor, we get

$$\vec{n} \times \vec{n} \times \vec{E}_1 - \bar{K}\cdot\vec{E}_1 = 0, \tag{2.5}$$

where $\bar{K}$ is the dielectric tensor and it is defined by [23]

$$\bar{K} = \frac{\bar{\varepsilon}}{\varepsilon_0} = \bar{I} + \frac{i}{\varepsilon_0\omega}\bar{\sigma}. \tag{2.6}$$

Applying vector identities on Eq. (2.5) and expressing it in matrix form, it yields to an homogeneous system of equations of the form $A\vec{x} = 0$, where in this case $\vec{x}$ corresponds to the perturbed electric field $\vec{E}_1$. Solving $\det(A) = 0$ is equivalent to solving the dispersion relation of the propagating wave $D(\omega,\vec{n}) = 0$. In general, this equation will have many solutions,

each one corresponding to a different mode. In order to solve it, a proper plasma model is needed to compute the conductivity tensor and find the explicit form of A.

2.2 The cold plasma model

The aim of this section is to compute the conductivity tensor $\bar{\sigma}$ by means of computing $\vec{J}$. Beginning with the momentum equations of the two-fluid model (electrons and ions), we have

$$m_e\left(\frac{\partial \vec{v}_e}{\partial t}+\vec{v}_e\cdot\nabla\vec{v}_e\right)=-e\left(\vec{E}+\vec{v}_e\times\vec{B}\right) \tag{2.7a}$$

$$m_i\left(\frac{\partial \vec{v}_i}{\partial t}+\vec{v}_i\cdot\nabla\vec{v}_i\right)=e\left(\vec{E}+\vec{v}_i\times\vec{B}\right). \tag{2.7b}$$

Assuming small perturbations and applying Fourier analysis as in the previous section, the momentum equations can be linearized to the first order and simplified. Assuming also that the wave is propagating in the x axis, then $k_x = k_\perp$. Doing some algebra, the resulting velocity components for both electrons and ions are:

$$v_x=\frac{q}{m}\frac{i\omega E_x-\omega_c E_y}{\omega^2-\omega_c^2}, \tag{2.8a}$$

$$v_y=\frac{q}{m}\frac{i\omega E_y+\omega_c E_x}{\omega^2-\omega_c^2}, \tag{2.8b}$$

$$v_z=\frac{iq}{m\omega}E_z. \tag{2.8c}$$

Recalling that $\vec{J}=en(\vec{v}_i-\vec{v}_e)$ and that $\vec{J}=\bar{\sigma}\vec{E}$ we can obtain the conductivity tensor $\bar{\sigma}$, from which the dielectric tensor is derived using Eq. 2.6:

$$\bar{K}=\begin{pmatrix} K_\perp & -iK_{xy} & 0\\ iK_{yx} & K_\perp & 0\\ 0 & 0 & K_\parallel \end{pmatrix} \tag{2.9}$$

where

$$K_\perp = K_{xx} = K_{yy} = 1 - \sum_j \frac{\omega_{pj}^2}{\omega^2 - \omega_{cj}^2}, \tag{2.10a}$$

$$K_\parallel = K_z = \sum_j \frac{\omega_{cj}\omega_{pj}^2}{\omega\left(\omega^2 - \omega_{cj}^2\right)}, \tag{2.10b}$$

$$K_{xy} = 1 - \sum_j \frac{\omega_{pj}^2}{\omega^2}. \tag{2.10c}$$

Here the sums are over all the ion species and electrons. When hot plasma effects are taken into account, the terms of $\bar{K}$ become more complicated and can be found in [3]. Now the roots for $n_\perp^2$ can be found by using the derived expression for the dielectric tensor $\bar{K}$. It can be seen that two different propagating modes arise: the slow wave or shear Alfvén mode (2.11a) and the fast magnetosonic wave or compressional Alfvén mode (2.11b):

$$n_{\perp_{SW}}^2 = \frac{\left(\varepsilon_\perp - n_\parallel^2\right)\varepsilon_\parallel}{\varepsilon_\perp} \tag{2.11a}$$

$$n_{\perp_{FW}}^2 = \frac{\left(\varepsilon_\perp - n_\parallel^2\right)^2 - \varepsilon_{xy}^2}{\varepsilon_\perp - n_\parallel^2}. \tag{2.11b}$$

2.3 Basic concepts on the wave propagation

In this section the basic concepts on wave propagation in a plasma are introduced. The aim is to discuss under which circumstances the wave can reach the region of interest in the plasma, that is the resonance region located at the center of the plasma, where heating occurs.

2.3.1 Cutoffs and resonances

Cutoffs and wave resonances deal with the limiting values of the wave vector k that alter dramatically the characteristics of a wave. To analyze such values of k, the dispersion relations found in section 2.1 are used.

A wave cutoff occurs when $k_\perp^2 = 0$, or equivalently, $n_\perp^2 = 0$. At this point the phase velocity becomes infinite, although the group velocity remains finite. Beyond this point, $k_\perp^2$ becomes negative, so the roots are imaginary. Hence, the wave becomes evanescent.

A wave resonance happens when $k_\perp^2 \to \infty$, where both the phase and group velocity tend to 0, which means that the energy flow slows down and large absorption occur. Nevertheless, if instead of using the cold plasma model the hot plasma effects are considered, it can be seen that kinetic effects cause wave resonances to vanish. Instead, mode conversions arise, where an incoming plasma wave is converted to another type of wave. Both waves are solutions of the dispersion relation with the same ω and $k_\parallel$, but with different $k_\perp$.

2.3.2 Accessibility

The region of interest for the wave to reach is the plasma center. Waves are launched from the antennas located at the outer wall (low-field side), i.e. at the plasma edge. The accessibility assesses the capability of a wave to reach the plasma center without encountering cutoffs.

The accessibility of both the slow and the fast magnetosonic waves is analyzed in [7] and in [8], where it is proved that only the fast magnetosonic mode can reach the resonance region.

2.3.3 Wave polarization

In plasma physics the polarization P is usually defined based on the fact of whether the wave electric field has or has not a parallel component to $\vec{B}$. If it does ($E_\parallel \neq 0$), the wave is classified as an ordinary wave or O-mode wave. If it does not ($E_\parallel = 0$), the wave is said to be an extraordinary wave or X-mode wave. In this kind of analysis it is convenient to introduce a new set of components for the transverse component of the electric field $E_\perp$ [22], that is E_+ and E_-. They specify the rotating direction of the electric field in the transverse plane, and they are defined as

$$E_\pm = \frac{1}{\sqrt{2}} \left(E_x \pm i E_y \right). \tag{2.12}$$

2.4 Damping mechanisms

Once the wave enters the plasma and reaches the strong absorption region, several damping mechanisms compete. Both ions and electrons are accelerated by both components of the wave electric field $E_\perp$ and $E_\parallel$, which results in the wave energy absorption by particles and hence the wave damping and background plasma heating. This section provides a brief discussion on such damping mechanisms in ICRF waves.

Charged particles can damp the energy of an EM wave by means of a resonance condition in the equation of motion. The condition of wave-particle resonance can be written as

$$\omega = k_{\|} v_{\|} + l\omega_c \qquad l = 0, 1, 2, \ldots \tag{2.13}$$

where $k_{\|} = \vec{k} \cdot \vec{B}/\|\vec{B}\|$ is the parallel component of the wave vector k to the background magnetic field B, $v_{\|} = \vec{v} \cdot \vec{B}/\|\vec{B}\|$ is the parallel component of the particles to $\vec{B}$ and $\omega_c = qB/m$ is the cyclotron frequency. Hence, resonance occurs when the Doppler-shifted frequency is equal to an exact harmonic of the cyclotron frequency. The $l = 0$ resonance corresponds to Landau damping, $l = 1$ to the heating at the fundamental frequency and $l > 1$ to higher harmonics. Since the cyclotron frequency ω_c is proportional to B and $B \propto B_0 R_0/R$ where R is the radius and B_0 is the magnetic field on axis, the position of the resonance layer can be controlled by changing the antenna frequency and magnetic field. Therefore, experiments with different resonant ion species can be carried out by tuning these parameters. Usually the position of the resonance region is tuned to be near the plasma center to achieve efficient heating. In Fig. 2.1 the resonant positions of several ion species for two different antenna frequencies and for $B_0 = 3.25$ T (typical JET parameters) are shown.

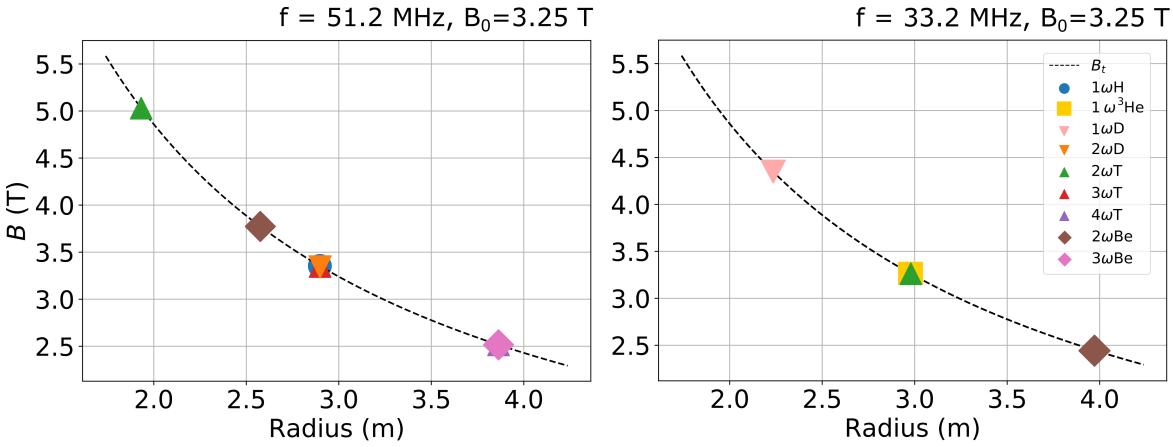

Fig. 2.1 *Resonance positions of different ion species and cyclotron harmonics for typical JET parameters of the antenna frequency and on-axis toroidal magnetic field* B_0.

Regarding wave polarization, discussed in section 2.3.3 and according to the direction of the cyclotron rotation for ions and electrons, it can be inferred that anticlockwise polarization (E_+) enhances ion absorption while clockwise polarization (E_-) enhances electron absorption. Therefore, in ICRH it will be interesting to have a strong E_+ component to maximize ion absorption. The consequences of this are further discussed in section 2.5.

2.4.1 Ion cyclotron resonance damping

Damping at the ion cyclotron resonance is produced when the wave-particle resonance condition is met. For example, assuming fundamental heating ($l = 1$) in ions and X-mode, and solving the differential equation, the solution of the velocity for ions reads

$$v_\perp = v_0 e^{-i\omega_c t} + \frac{eE_+}{m} t e^{-i\omega_c t}. \tag{2.14}$$

As the two terms are in phase, there will be a net acceleration. However, this is only true for small Larmor radius r_L compared to the wavelength λ. If this is not the case, the space dependence of the electric field must be considered, which means that it changes along the cyclotron trajectory. This is called the finite Larmor radius effect (FLR), and it implies that the particle can be either accelerated or decelerated by E_+. Besides, for $\lambda > r_L$, E_- can also produce absorption. The kick in the perpendicular velocity considering FLR effects reads [5]

$$\Delta v_\perp \propto \left[E_+ J_{l-1}\left(\frac{k_\perp v_\perp}{\omega_{ci}}\right) + E_- J_{l+1}\left(\frac{k_\perp v_\perp}{\omega_{ci}}\right)\right], \tag{2.15}$$

where J_l is the Bessel function of the first kind and the subscript l is the cyclotron harmonic number. The implications of Eq. 2.15 give a lot of insight to the physics involved in ICRH. For instance, it can be deduced that for fundamental heating ($l = 1$) the kick in the perpendicular velocity is somewhat uniform in the velocity space. On the other hand, for higher harmonics ($l \geq 2$), the low energy ions do not experience a strong kick, so ICRH is not very effective in bulk ions under these conditions. Besides, the damping strength decreases when the harmonic number increases. These ideas are further discussed in chapters 4 and 5.

2.4.2 Direct electron damping

Regarding wave damping by electrons, two main mechanisms compete and counteract each other: electron Landau damping (ELD) and transit time magnetic pumping (TTMP).

Landau damping consists in the absorption of the wave energy by electrons that fulfill $\omega \approx v_{\parallel e} k_\parallel$, or equivalently, $l = 0$ in the resonance condition. That is, the electrons that have a velocity close to the phase velocity of the wave experiment a net acceleration by $E_\parallel$ which makes the wave to damp. In the ICRF regime, nevertheless, $E_\parallel$ is small, so Landau damping is weak.

On the other hand, the gyro motion of the electrons in a magnetic field has an associated magnetic moment. This causes electrons to be accelerated by the parallel gradient of the wave magnetic field and hence the wave is also damped. This is the TTMP mechanism.

2.5 Heating schemes with ICRF waves

As discussed in section 2.3.2, only fast waves have a good accessibility to the strong absorption region. Moreover, in ICRH the wave is interesting to be left-circularly polarized in order to boost ion absorption. Typically, a fast wave that reaches the absorption region is elliptically polarized. The fraction of power absorbed will therefore depend on the ratio E_+/E_-. For fast magnetosonic waves and a single ion species, assuming $n_\parallel \approx 0$ and $E_\parallel \approx 0$, the ratio reads

$$\frac{E_+}{E_-} \approx \frac{\omega - \omega_{ci}}{\omega + \omega_{ci}}. \tag{2.16}$$

It is quickly seen that for fundamental heating ($\omega = \omega_{ci}$), the wave is completely rotating clockwise or, in other words, has an "exactly wrong" polarization [7], so absorption is very weak. Therefore, other heating schemes must be explored.

There are several ways to overcome this setback. One of these options is, for instance, heating at higher harmonics ($\omega = l\omega_{ci}$ with $l \geq 2$), since it can be easily seen from Eq. 2.16 that in such a case a fraction of left polarized wave is kept. In this case good accessibility remains and the damping rate is large enough to be considered a satisfactory heating, although it loses robustness because of a large sensitivity to temperature and density. This lack of robustness can be relieved by adding a small population of a different ion species with a higher cyclotron frequency than the D cyclotron frequency ω_{cD}. Such species may be H ($\omega_{cH} = 2\omega_{cD}$) and ^{3}He ($\omega_{cHe} = (4/3)\omega_{cD}$). The idea is to choose the wave frequency so that it corresponds to the fundamental of the minority species. This way the polarization issue is overcome, since the dispersion relation is mainly determined by the majority species. The minority species, when heated, transfer the energy to the bulk plasma via collisions (see section 2.6.1).

2.6 The distribution function

In order to fully describe a plasma, one should solve the equation of motion ($\vec{F} = m\ddot{\vec{x}}$) for every particle. As a plasma is composed by a large number of them, this is unfeasible from both, the analytical and computational point of view. That is why a macroscopic approach is taken by using a distribution function $f(\vec{r},\vec{v},t)$, which expresses the particle density in a six-dimensional space $\int d^3r\, d^3v f = N$. If normalized, it describes the probability of finding a particle in the volume $d^3r\, d^3v$.

ICRH does modify the distribution function. The time evolution of $f(\vec{r},\vec{v},t)$ will be governed by the Boltzmann equation, which in plasma physics reads [18]

$$\frac{\partial f}{\partial t}+\vec{v}\cdot\vec{\nabla}f+\frac{Ze}{m}\left(\vec{E}+\vec{v}\times\vec{B}\right)\cdot\vec{\nabla}_v f=-\frac{\partial}{\partial v_i}\left(\langle\Delta v_i\rangle f\right)+\frac{1}{2}\frac{\partial^2}{\partial v_i\partial v_j}\left(\langle\Delta v_i\Delta v_j\rangle f\right), \quad (2.17)$$

where the third term includes particle acceleration due to Lorentz force and the Fokker-Planck right-hand term represents the collisional effects. The quantities in brackets stand for mean values during a time Δt and they correspond to the friction coefficient ($\langle\Delta v_i\rangle$) and the diffusion coefficient ($\langle\Delta v_i\Delta v_j\rangle$).

2.6.1 Collisional heating

When ions are accelerated by ICRH power they slow-down via Coulomb collisions, which are elastic collisions between two charged particles that interact through their own electric field. They can collide, however, with both ions and electrons. The threshold energy that determines if ion-ion collisions are more frequent than ion-electron collisions is called the critical energy, and it reads [21]

$$E_{crit}=14.8AT_e\left[\sum_j\frac{n_jZ_j^2}{n_eA_j^2}\right]^{\frac{2}{3}}. \quad (2.18)$$

Here A is the atomic number, T_e is the electron temperature and the sum is over all the thermal ion species. If $E_i<E_{crit}$ ions will collide with ions more frequently, while if $E_i>E_{crit}$ they will do so with electrons. In the latter case, as ions are more massive, they will hardly be deflected after the collision and therefore the pitch angle ($\cos(\theta)=v_\parallel/v$) will remain constant, while in the former case both pitch angle scattering and energy diffusion are important. Thus, keeping ions at a lower energy than E_{crit} is crucial to perform proper bulk ion heating.

2.6.2 Thermal and fast ions

The distribution function of species j in thermodynamic equilibrium is described by a Maxwellian

$$f_j(\vec{r},\vec{v},t)=n_j\left(\frac{m_j}{2\pi T_j}\right)^{\frac{3}{2}}\exp^{-m_jv^2/2T_j} \quad (2.19)$$

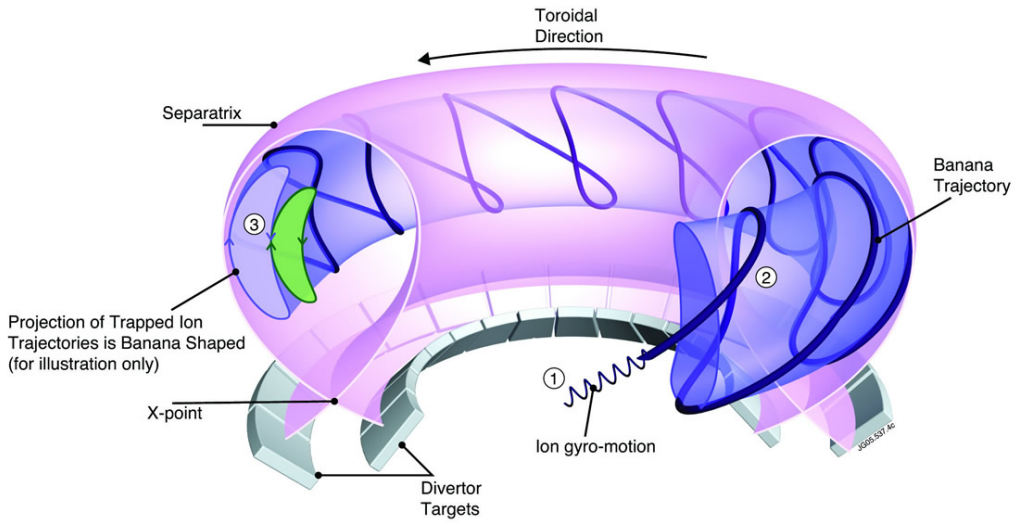

Fig. 2.2 *Illustration of banana orbits followed by trapped particles (courtesy of EUROfusion). Notice that ion cyclotron motion still exists, although at a smaller spatial scale than that of banana orbits.*

Nevertheless, when applying ICRH, the system can be out of equilibrium and the distribution function can become non-Maxwellian. This is due to the fact that the collision frequency decays with velocity as v^{-3}. When the perpendicular velocity $v_\perp$ of the ions is increased by ICRF waves, the collisions are not fast enough and the slowing-down time strongly increases. This makes the distribution function develop a high-energy tail with a large population of trapped ions.

These trapped particles are called the fast ions, and they have quite a different behaviour than thermal ions. For instance, their trajectories become more exotic, as seen in Fig. 2.2 since they can experience an orbit shift and no longer remain in the same magnetic flux surface. The model used in this thesis takes into account these effects in a simplified way. Fast ions are also responsible of many radial transport phenomena across magnetic surfaces, although this is out of the scope of this thesis. The fusion reactions that involve such fast ions are said to be non-thermal, while thermal reactions stand for the ones that involve only bulk ions that are governed by the Maxwellian part of the distribution function.

Chapter 3

Modelling of ICRF heating with the PION code

3.1 Introduction to the PION code

Modelling of plasma heating in tokamaks is essential to study the absorption of resonant species and the evolution of their velocity distribution function. This allows to compute relevant magnitudes such as the neutron yield, the plasma energy and the ion-ion interactions subject to external conditions such as ICRF heating.

In the present work, in order to analyze the experiments carried out at JET, the PION code [6] has been used. It is based on a simplified wave model to compute the propagation of a wave in the plasma, since a full-wave model would involve large CPU required times. Despite these simplifications, the results have been proved to be robust as they have been used and benchmarked against several important tokamak experiments [10, 15, 20].

Now that all the reactor-related concepts and the physics of ICRH have been introduced, we can describe the procedure that PION follows to model ICRH. At every time step, PION computes the power deposition i.e. the absorption of the wave by ions and electrons. Then, the evolution of the pitch angle velocity distribution function is calculated by means of solving the 1D Fokker-Planck equation. These two procedures are coupled by computing the dielectric tensor components including the effects of fast ions, obtained using the results of the Fokker-Planck calculation and used in the power deposition and to solve the dispersion relation. Besides, only the fast magnetosonic mode is assumed to propagate in the plasma in PION, with no mode conversion conditions considered. In this chapter a brief explanation on how all these steps are performed is provided.

3.2 Brief description of the procedure

3.2.1 Modelling of the velocity distribution function. Fokker-Planck calculation

The time evolution of the velocity distribution function can be described by a Fokker-Planck equation

$$\frac{df}{dt} = C(t) + Q(t) + S, \tag{3.1}$$

where $C(t)$ is a collisional operator, $Q(t)$ a quasi-linear operator describing the wave-particle interaction and S is a source term which takes into account the NBI and the losses. Assuming small orbits, the equation is two-dimensional having the magnetic moment and the velocity as constants of motion. Nevertheless, in PION, the two dimensional form of the equation is not solved. In order to reduce computing time, an approximate equation for the pitch angle-averaged distribution function is solved instead,

$$\frac{df}{dt} = \frac{1}{v^2}\frac{\partial}{\partial v}\left[-\alpha v^2 f + \frac{1}{2}\frac{\partial}{\partial v}\left(\beta v^2 f\right)\right] + \frac{1}{v^2}\frac{\partial}{\partial v}\left[v^2 D_{RF}\frac{\partial f}{\partial v}\right] + S, \tag{3.2}$$

where the collision coefficients α and β can be found in [13]. The diffusion coefficient D_{RF} can be written in the general form as

$$D_{RF} = \sum_N K\left|J_{n-1}\left(\frac{k_\perp v_\perp}{\omega_{ci}}\right) + \frac{E_-}{E_+}J_{n+1}\left(\frac{k_\perp v_\perp}{\omega_{ci}}\right)\right|^2, \tag{3.3}$$

where n is the harmonic of the cyclotron frequency at which the interaction takes place, K is a constant proportional to $|E_+|^2$ and the sum is over the propagating wave modes. At every time step, the new distribution function is computed, from which some magnitudes of interest are obtained. For instance, in the power deposition computing stage, the averaged square parallel velocity $\langle v_\parallel^2\rangle$ is needed, and it is computed as follows:

$$\langle v_\parallel^2\rangle = \frac{\int \mu_{\text{eff}}^2 v^2 f(v) dv}{\int v^2 f(v) dv}, \tag{3.4}$$

where the effective pitch angle is, approximately

$$\mu_{\text{eff}}^2 = \frac{1}{3}\frac{1+(v/v_*)^2}{1+(v/v_*)^2+(v/v_*)^4}, \tag{3.5}$$

with $v_* = 0.5v_\gamma$ and v_γ being a characteristic velocity associated with pitch angle scattering and is defined in [2].

3.2.2 Modelling of power deposition

By solving the wave equation, the wave propagation, coupling and absorption can be modelled. Let us assume for now that the components of the dielectric tensor $\bar{\varepsilon}$ are known. Applying the simplified model, the power deposition algorithm is based on the Fourier decomposition of the wave in the toroidal direction and the calculation of the power deposition for each mode. One can think of the wave field as the superposition of two components, one in the limit of strong absorption and one in the limit of weak absorption. To calculate the power deposition, a Fourier decomposition in the toroidal direction of the wave is performed, and then the flux surface averaged Poynting vector is computed for each mode N using

$$P(s) = \int_0^s p_{\mathrm{ICRF}}(s')d^3x = \alpha P_s(s) + (1-\alpha)P_w(s), \tag{3.6}$$

where $P_s(s)$ and $P_w(s)$ correspond to the strong and weak absorption components and s is a flux surface label defined as

$$s = \sqrt{\frac{\psi - \psi_0}{\psi_a - \psi_0}}. \tag{3.7}$$

Here ψ stands for the poloidal magnetic flux and the subscripts a and 0 correspond to the plasma edge and the magnetic axis, respectively. As explained in section 1.3.3 the geometry of the flux surfaces makes that the flux surface label can be understood as a modified radial coordinate with the origin at the plasma center.

One of the constants of interest to be computed is α, which is found through the relation $\alpha = a_s^2(2-a_s)$, being a_s the single-pass absorption coefficient defined by

$$a_s = \frac{\omega}{2\pi P_x}\int \mathrm{Im}(\vec{E}^* \cdot \bar{\varepsilon} \cdot \vec{E}), \tag{3.8}$$

where P_x is the incoming Poynting flux.

The two components of the flux surface averaged Poynting vector $P_s(s)$ and $P_w(s)$ are computed for all resonating ion species and electrons, so $P_s(s) = \sum_j P_{sj}(s, N, \langle v_{\|j}^2 \rangle)$ and $P_w(s) = \sum_j P_{wj}(s, a_j(s), F(s))$. Here $\langle v_{\|j}^2 \rangle$ is the average for the square parallel velocity of the resonating ion species j, $a_j(s)$ is the absorption coefficient for species j and $F(s)$ is the averaged electric wave field strength along the cyclotron resonance in the limit of weak

absorption. In order to compute the absorption coefficients $a_j(s)$ the Wentzel-Kramers-Brillouin (WKB) approximation is used, yielding

$$a_j = \int_{-\infty}^{\infty} \left\{ \frac{k_0^2}{|k_\perp|} \mathrm{Im}(\varepsilon_{xx}^j) \left| \frac{\varepsilon_{xy}}{\varepsilon_{xx} - n_\parallel^2} \right|^2 + \mathrm{Im}(\varepsilon_{yy}^j) + 2\mathrm{Re}(\varepsilon_{xy}^j) \mathrm{Im}\left(\frac{\varepsilon_{xy}}{\varepsilon_{xx} - n_\parallel^2} \right) \right\} \cdot \exp\left\{ - \int_{-\infty}^{x} 2\mathrm{Im}\left(k_\perp(x')\right) dx' \right\} dx. \tag{3.9}$$

Finally $P(s)$ is computed and, from it, the local flux surface averaged power density

$$p_{\mathrm{ICRH}}(s) = \frac{dP(s)}{ds} / \frac{dV}{ds}, \tag{3.10}$$

where V is the plasma volume.

3.2.3 Modelling of the dielectric tensor

The dielectric tensor is needed to compute the power deposition as seen in section 3.2.2, and it depends on the velocity profiles and gradients computed in the Fokker-Planck equation. A simplified model is used to compute its components [6], in which three parameters ($\gamma_{+,N}^j$, $\gamma_{-,N}^j$ and $\gamma_{c,N}^j$) together with $\langle v_\parallel^2 \rangle$ are needed. To calculate the γ parameters, the diffusion tensor for RF heating D_{RF} must be computed. It can be divided in three components defined as:

$$D_{RF,N}^{+} = K_N \left| J_{n-1}\left(\frac{k_\perp v_\perp}{\omega_{ci}} \right) \right|^2 \tag{3.11a}$$

$$D_{RF,N}^{-} = K_N \left| \frac{E_-}{E_+} J_{n+1}\left(\frac{k_\perp v_\perp}{\omega_{ci}} \right) \right|^2 \tag{3.11b}$$

$$D_{RF,N}^{c} = 2K_N \left| \frac{E_-}{E_+} J_{n+1}\left(\frac{k_\perp v_\perp}{\omega_{ci}} \right) J_{n-1}\left(\frac{k_\perp v_\perp}{\omega_{ci}} \right) \right|^2, \tag{3.11c}$$

where N stands for the toroidal mode, n corresponds to the cyclotron harmonic and J_i are the Bessel functions of the first kind. The power density absorbed due to D_{RF} by species j and toroidal mode N can be computed as:

$$p_{\sigma,N}^j = 2\pi m \int_0^\infty \frac{1}{v^2} \frac{\partial}{\partial v} \left(v^3 D_{RF,N}^\sigma \right) f_j v^2 dv \qquad \sigma = +, -, c. \tag{3.12}$$

where f_j is the pitch angle velocity distribution function of species j. Then, the γ factors are defined as:

$$\gamma^j_{+,N} = \frac{p^j_{+,N}}{p^{j,M}_{+,N}}, \gamma^j_{+,N} = \frac{p^j_{-,N}}{p^{j,M}_{-,N}}, \gamma^j_{+,N} = \frac{p^j_{c,N}}{p^{j,M}_{c,N}} \tag{3.13}$$

where the superscript M stands for the power absorbed by a Maxwellian distribution with the same density as the actual distribution function. The γ factors represent the ratios between the actual absorbed power densities and the power densities that would be absorbed by a Maxwellian distribution.

Now, according to the electromagnetic theory and neglecting the contribution of the parallel electric field, the local absorbed power can be written as

$$\begin{aligned} p^j_{RF} = \frac{\omega}{2\pi}\left(\vec{E}^* \cdot \bar{\varepsilon} \cdot \vec{E}\right) = \frac{\omega}{2\pi}\{\|E_+\|^2 \left[\mathrm{Im}\left(\varepsilon^j_{xx} + \varepsilon^j_{yy}\right) - 2\mathrm{Re}\ \varepsilon^j_{xy}\right] \\ + \|E_-\|^2 \left[\mathrm{Im}\left(\varepsilon^j_{xx} + \varepsilon^j_{yy}\right) + 2\mathrm{Re}\varepsilon^j_{xy}\right] + 2\mathrm{Re}\left(E_+ E^*_-\right) \mathrm{Im}\left(\varepsilon^j_{xx} - \varepsilon^j_{yy}\right)\}. \end{aligned} \tag{3.14}$$

The absorption strength in the power deposition calculation must be consistent with that in the Fokker-Planck calculation. Hence, the following relations must hold, from which the anti-Hermitian parts of the dielectric tensor $\mathrm{Im}(\varepsilon^j_{xx})$, $\mathrm{Im}(\varepsilon^j_{yy})$ and $\mathrm{Re}(\varepsilon^j_{xy})$ can be found in terms of the γ factors:

$$\mathrm{Im}\left(\varepsilon^j_{xx} + \varepsilon^j_{yy}\right) - 2\mathrm{Re}\left(\varepsilon^j_{xy}\right) = \gamma^j_{+,N}\left[\mathrm{Im}\left(\varepsilon^{j,M}_{xx} + \varepsilon^{j,M}_{yy}\right) - 2\mathrm{Re}\left(\varepsilon^{j,M}_{xy}\right)\right] \tag{3.15a}$$

$$\mathrm{Im}\left(\varepsilon^j_{xx} + \varepsilon^j_{yy}\right) + 2\mathrm{Re}\left(\varepsilon^j_{xy}\right) = \gamma^j_{-,N}\left[\mathrm{Im}\left(\varepsilon^{j,M}_{xx} + \varepsilon^{j,M}_{yy}\right) + 2\mathrm{Re}\left(\varepsilon^{j,M}_{xy}\right)\right] \tag{3.15b}$$

$$\mathrm{Im}\left(\varepsilon^j_{xx} - \varepsilon^j_{yy}\right) = \gamma^j_{c,N}\left[\mathrm{Im}\left(\varepsilon^{j,M}_{xx} - \varepsilon^{j,M}_{yy}\right)\right]. \tag{3.15c}$$

Here the Maxwellian contributions to the dielectric tensor can be found in textbooks. The corrections in the Hermitian part of the dielectric tensor are more difficult to calculate and can be found in [6].

With the components of the dielectric tensor known, the wave equation can be solved so that the wave propagation and absorption (i.e. the dispersion relation) can be computed.

Chapter 4

High performance D discharges at JET

4.1 Introduction

In the present tokamak experiments, including the ones performed in JET, the plasmas are produced by discharges that last a few seconds. The procedure to carry out a discharge is the following [1]: After the vacuum is created in the vacuum vessel, the external magnetic field is set up and a current is applied in the inner poloidal field coils. The gas is then puffed inside the vessel and the discharge is triggered by slowly reducing the current in the transformer and hence inducing a peripheral voltage. The plasma is produced when the gas gets ionized and its geometric characteristics are adjusted with a feedback-control system. When the current density is at steady state, the heating phase begins. Plasma discharges in tokamaks eventually get to an end because the minimum current in the transformer coil is reached and flux change is no longer possible, so the plasma current also decreases in time. A discharge can be terminated due to MHD activity [15] or due to the presence of high-Z impurities that increase radiation losses [8]. These mechanisms can cause a deterioration of the confinement and ultimately lead to the plasma loss.

Plasma discharges are performed in the context of campaigns that work with particular plasma configurations and have specific aims. The present campaign is centered on the study of D plasmas in preparation for the next D-T campaign as explained in section 1.5. In this context, a high performance discharge stands for an experiment whose plasma configuration is capable of supplying a significantly high neutron yield.

In this chapter, two discharges of the present campaign (No. 96482 and No. 96947) are modelled numerically. Once the results are validated with experimental data, the two discharges are studied with the focus on the heating performance. The latter has achieved

[1] Max-Planck Institut für Plasmaphysik (https://www.ipp.mpg.de/en)

a record neutron yield of $5 \cdot 10^{16}$ s^{-1}, which was one of the aims of the present campaign. Besides, to compare certain features with different heating schemes, discharge No. 94671, which belongs to an earlier campaign, is also studied.

The discharges are modelled using the ICRF code PION. PION is fed with data from the CHAIN2 JET database, from which it gets the temperature and density profiles, the magnetic equilibrium and the NBI and ICRH applied power. As described in chapter 3, the code computes the distribution function and the power absorbed from ICRF waves by the plasma, among others. The provided results will be used to assess the heating characteristics of the high performance discharges and some of its main features regarding the achieved neutron yield.

The simulations performed for this chapter correspond to the main phase of the experiments, when the plasma discharge takes place and the heating mechanisms are activated. The previous stages of the experiments are not contemplated in the time axes.

4.2 Analysis of H minority high performing discharges

One of the most promising heating schemes in high performance discharges is H minority heating. In fact, the record discharges 96482 and 96947 both had a small H population in the plasma. While discharge 96482 demonstrated high performance most of the time, discharge 96947 showed two different regimes: the first phase corresponds to a high performance regime where a record neutron yield of $5 \cdot 10^{16}$ neutrons/s was achieved. Then a low performance phase followed due to impurity accumulation and confinement loss. They featured a toroidal magnetic field of $B_T = 3.25$ T and 3.2 T and a plasma current of $I_P = 2.7$ MA and 2.3 MA, respectively. The antenna frequency in both cases was set to $f = 51.2$ MHz, which corresponds to central resonance of the H fundamental cyclotron frequency and, consequently, also with the second harmonic of the D cyclotron frequency, i.e. $\omega = \omega_H = 2\omega_D$ (see Fig. 2.1). The D beam energies were set to ~ 110 keV. In Fig. 4.1 an overview of these discharges is shown including the most interesting parameters of the discharge for our analysis. The displayed data corresponds to experimentally measured parameters provided by the JET database.

4.2.1 Validation of the model

Before assessing the physics behind H minority heating, we compare the results of PION against the collected experimental data in order to validate the current models that are assumed in the code. To do so, the neutron yield is computed with PION in both discharges

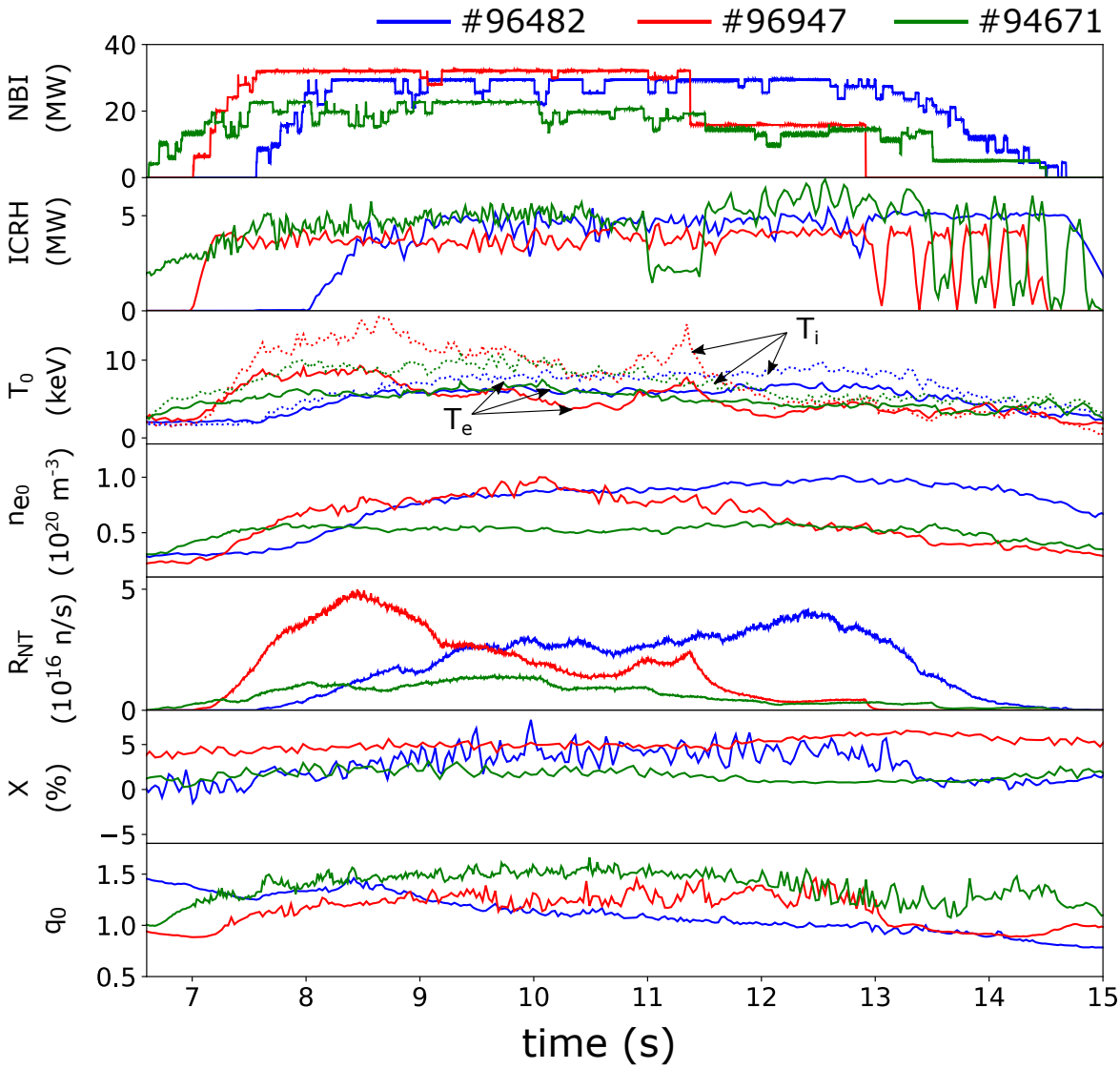

Fig. 4.1 *Overview of the H minority discharges* 96482 *(blue) and* 96947 *(red) and the* ^{3}*He minority discharge* 94671 *(green). From top to bottom, the input NBI heating power, the input ICRH power, the central electronic (solid) and ionic (dotted) temperatures, the central plasma density, the neutron rate production, the minority concentration and the safety factor q at the center.*

by taking the experimental data of background plasma parameters such as the electronic temperature T_e and minority concentration. The ion temperature T_i must be also computed through experimental procedures by using the ratio between the ion and electron temperatures T_i/T_e, which is measured experimentally with X-ray spectroscopy. The results show that this ratio is around $1.25-1.4$ and $1.5-1.8$ for discharges 96482 and 96947 respectively. The H concentration (expressed as $n_H/(n_H+n_D)$) is also measured experimentally. As seen in Fig.

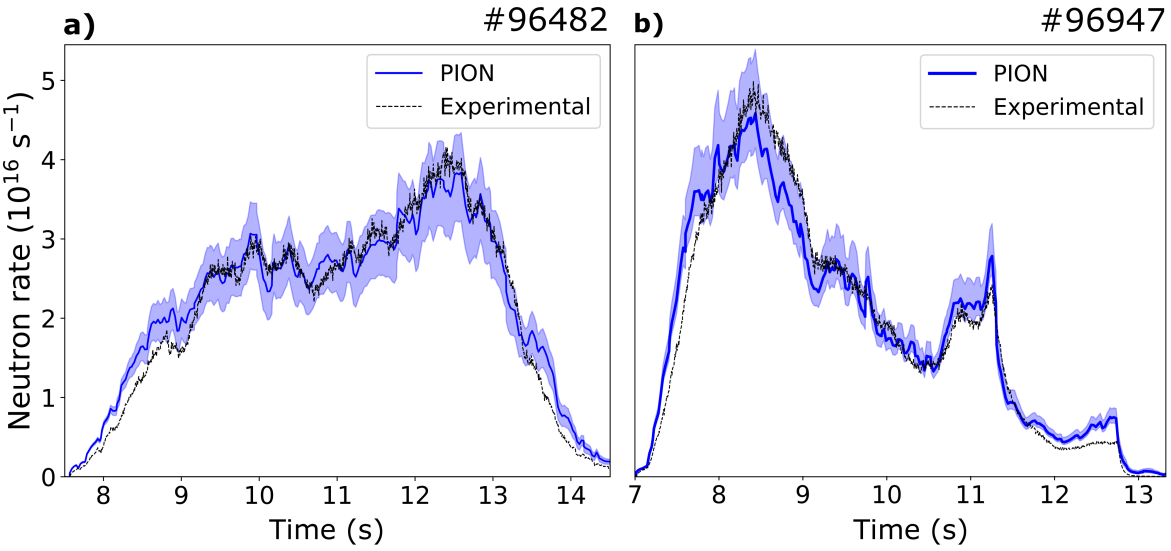

Fig. 4.2 *Experimental (black dotted) and modelled (blue solid) neutron rate production of discharges* 96482 *(a) and* 96947 *(b). The shaded area indicates the accepted uncertainties in temperature and density measurements.*

4.1 its measurement can be quite noisy as in the case of discharge 96482, so the validation is also useful to narrow down the range of possible H concentrations. The concentrations have been assumed to be $\sim 2.25\%$ and $\sim 4.5\%$ respectively, and an uncertainty of $\pm 1.5\%$ associated with the experimental measurements has been considered. The neutron yield computed by PION in both discharges shows good agreement with the experimental data as seen in Fig. 4.2. All the results taking into account the uncertainties in the temperature ratio and impurity concentration fall into the shaded area, and the solid line corresponds to the parameters in these ranges that have been considered to be in best agreement so that they have been used to analyse the heating performance.

4.2.2 RF absorption in H minority discharges

One of the aims of this section is to analyze the role of an H minority population in the absorption of RF waves in a tokamak plasma. In the D plasmas of the present discharges three competing absorption mechanisms are expected to be encountered: Direct electron damping, fundamental H damping and 2^{nd} D harmonic damping. The results obtained with PION in both discharges are shown in Fig. 4.3.

Regarding the absorption of the wave on ion cyclotron harmonics, it is important to understand the implications of the formula of the velocity kick introduced in chapter 2 (Eq. 2.15). In the present cases, the Bessel functions that appear in Eq. 2.15 are J_0 and J_2 for fundamental H absorption and J_1 and J_3 for 2^{nd} D harmonic absorption. The main difference

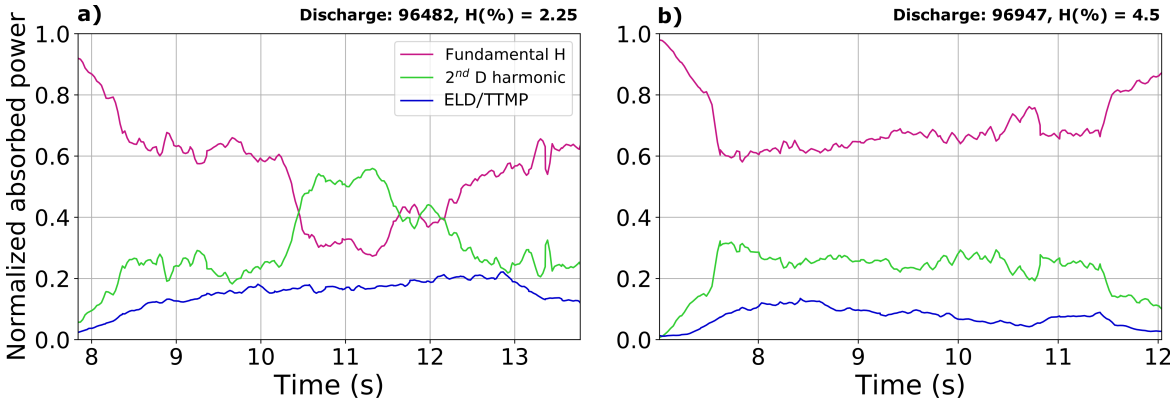

Fig. 4.3 *Normalized RF power absorption mechanisms throughout the discharges a)* 96482 *($P_{ICRH} = 5MW$) and b)* 96947 *($P_{ICRH} = 4MW$), fundamental H, 2nd D harmonic and direct electron damping*

is that only J_0 has a non zero value at low energies so H will be heated for all the energy spectrum that exists in the plasma. On the contrary, only energetic deuterons will absorb a significant amount of RF waves since J_1 peaks at higher energies. According to this, during the ramp-up phase, when ICRH is on but NBI is still not acting, fundamental H damping is predicted to be particularly important since it will absorb the wave power even when the ions are still "cold". On the other hand, 2$^{\text{nd}}$ harmonic will be relevant for energetic D ions. Therefore, during the main heating phase when NBI is turned on and bulk ion temperature has been raised via H collisional heating, an energetic D tail in the range of keV may appear in the distribution function which, eventually, could develop until the MeV range.

During the main heating phase, the wave power is practically entirely absorbed by the plasma. Therefore, the ion cyclotron absorption of fundamental H and 2$^{\text{nd}}$ D compete, in addition to electron absorption. The local power partition between 2$^{\text{nd}}$ D harmonic and H fundamental can be approximated by computing the second moment of the Fokker-Planck RF operator and keeping the lowest order term in the Taylor expansion as done in [14]:

$$\frac{p_2}{p_1} = c_{21}\frac{k_\perp^2 w_2}{n_1 m_1 \omega_{c2}^2}. \tag{4.1}$$

Here the subscripts 1 and 2 refer to H and D, respectively, p_1 and p_2 are the local power densities of H and D respectively, c_{21} is a constant computed experimentally ($\sim 0.2-0.3$ according to PION calculations), w_2 is the D energy density, n_1 and m_1 are the H density and mass, respectively, and ω_{c2} is the D cyclotron frequency. The power partition indicates how much wave power is absorbed by each ion species. Notice that the larger is the energy density of D, the more wave it will absorb, which is coherent with the previous reasoning. On the other hand, the minority density also plays a crucial role, as large H densities imply that

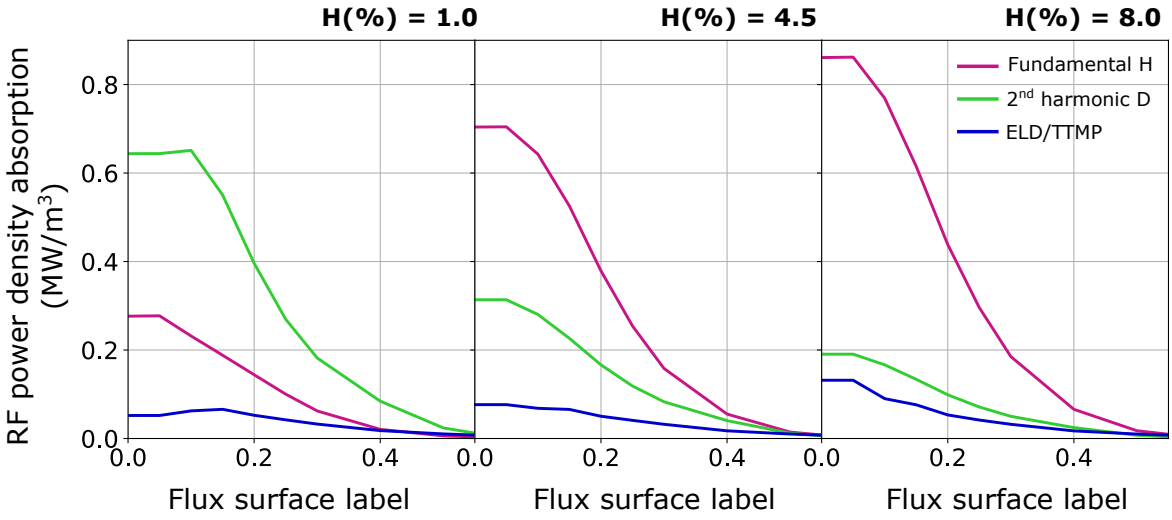

Fig. 4.4 *RF power absorption profiles for fundamental H (purple), 2nd D harmonic (green) and direct electron damping (blue) at $t = 8.47$s of discharge* 96947 *for different H minority concentrations.*

more wave power will be deposited mostly on H ions. This explains the behaviour observed in both discharges as seen in Fig. 4.3, where 2nd D damping dominates during the main heating phase in discharge 96482 where the H concentration is lower, while in discharge 96947 fundamental H damping is the most important mechanism during the whole discharge. Direct electron damping is also present in both cases, being of $\sim 15-20\%$ in discharge 96482 and $\sim 5-10\%$ in discharge 96947.

4.2.3 Impact of channeling the wave power to D ions and non-thermal reactions

The fusion reaction rate in D plasmas can be expressed as [7]

$$R_{DD} = \frac{1}{2}\int f(v_1) f(v_2) \sigma_{DD}\left(|v_1 - v_2|\right) |v_1 - v_2| \, dv_1 dv_2 \tag{4.2}$$

where $f(v_i)$ stands for the velocity distribution function of D. As seen in Fig. 1.1, the D-D fusion cross-section, σ_{DD}, is larger for energies at the MeV range. Accordingly, in this case, the more energetic are the deuterons, the higher will be the number of fusion reactions. Therefore, it is interesting that in D plasmas most of the heating power is channeled to D in order to achieve a strong energetic tail and increase the number of non-thermal reactions.

To confirm this hypothesis, three simulations of discharge 96947 have been performed keeping the same parameters except for the H concentration. In Table 4.1 the maximum fusion power achieved is shown, while Fig. 4.4 shows the absorption profiles at $t = 8.47$s,

H concentration (%)	1.0	4.5	8.0
Max. neutron yield (10^{16} n/s)	5.37	4.58	4.20

Table 4.1 *Maximum simulated neutron yield of discharge* 96947 *for different H concentrations*

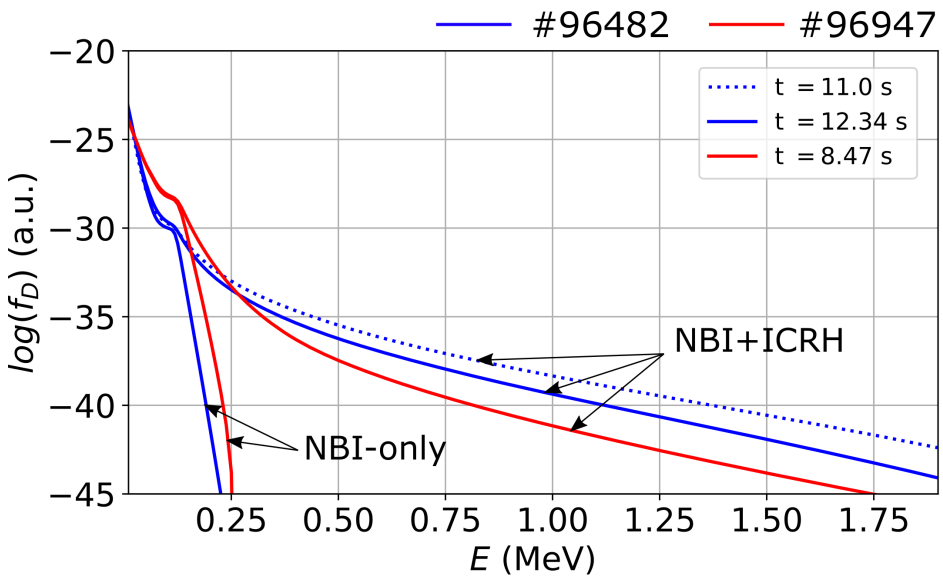

Fig. 4.5 *Distribution function of D at the plasma center of discharge* 96482 *(blue) at* $t = 11s$ *(dashed) and* $t = 12.34s$ *(solid), and discharge* 96947 *(red) at* $t = 8.47s$*. Notice the shoulder at energies* $\sim 110keV$ *corresponding to the NBI injected particles*

where this maximum is achieved. Here the flux surface label is defined in Eq. 3.7. It can be seen that for low minority concentrations, where the absorbed RF power by D is greater than the power absorbed by H, the fusion yield is the highest of the three. For high concentrations, the opposite situation happens, that is H absorbs most of the RF power and the fusion yield is not that high. Actually, the neutron rate production achieved with a 1% H concentration is $\sim 30\%$ higher than the achieved with a H concentration of 8%.

Knowing this, let us assess the impact of non-thermal reactions in the studied discharges. In Fig. 4.5 the distribution functions of D at the plasma center of discharges 96482 and 96947, with H concentrations of $\sim 2.25\%$ and $\sim 4.5\%$, respectively, are shown. Different runs have been also performed assuming NBI-only heating and full heating (NBI+ICRH). Discharge 96482 is studied at two time points of the high performance regime, at $t = 11.0$s, where D absorption is stronger than H absorption, and at $t = 12.34$s, where the neutron yield is maximum. Discharge 96947 is only analyzed at $t = 8.47$s, where the neutron yield peaks, as thereafter it enters to a low performance phase. Notice the effect of ICRH, which causes an

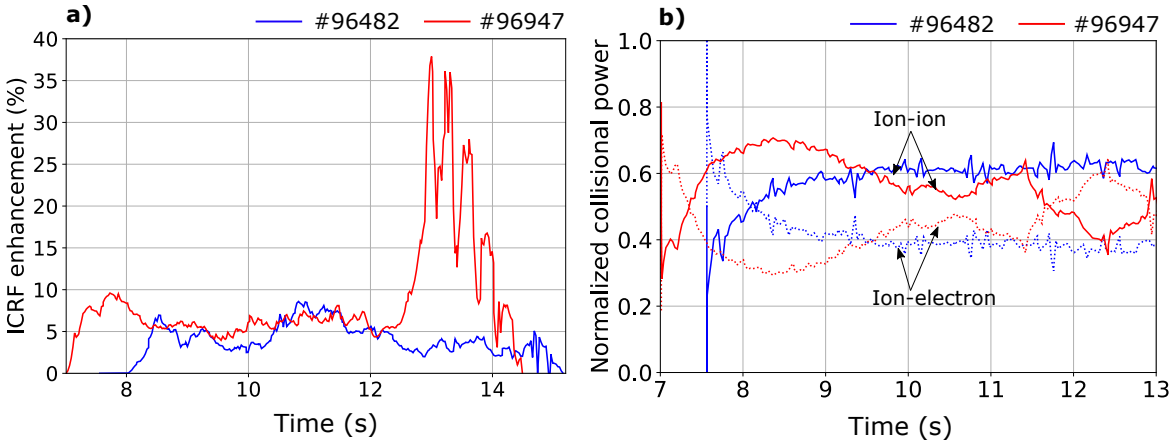

Fig. 4.6 *a) ICRF fusion enhancement and b) Net normalized collisional power transferred from fast ions to bulk ions (solid) and from fast ions to electrons (dotted) for discharges* 96482 *(blue) and* 96947 *(red).*

energetic tail to grow. In NBI-only cases, the most energetic particles are only slightly above the beam energies at $\sim$ 100 keV and a tail is not appreciated in the distribution function.

In the case of discharge 96482 with full heating, different tail strengths can be observed in the two studied time slices. This behaviour can be strongly related with D absorption shown in Fig. 4.3, as the more wave power is absorbed by D, the more the tail develops.

Comparing both discharges at the time where their respective maximum neutron yield is reached, it can be seen that more energetic ions are present in discharge 96482 than in 96947, where the H concentration is lower and then 2^{nd} D harmonic absorption is more powerful according to our previous analysis. Therefore, the absolute number of non-thermal reactions is expected to be larger in discharge 96482 as compared to discharge 96947.

To analyze the relative contribution of non-thermal reactions to the overall fusion yield of both discharges we can calculate the ICRF fusion enhancement. It is defined as the difference in % between the neutron yield calculated taking into account the full heating power and the one calculated with NBI-only heating, i.e. $\frac{R_{NT}(ICRH+NBI)-R_{NT}(NBI)}{R_{NT}(ICRH+NBI)}$. The thermal reactions are not reflected here since they cancel out. The ICRF enhancement of both discharges appear to be quite similar of around $5-10\%$ during the main heating phase (see Fig.4.6a).

4.2.4 Impact of thermal reactions and bulk ion heating

Our previous reasoning on the impact of non-thermal reactions contradicts the JET experimental diagnostics, as discharge 96947, where a lower absolute number of non-thermal reactions take place, achieves a higher neutron rate than 96482. This is partly explained by the high plasma density in both cases ($n_e \sim 10^{20}\text{m}^{-3}$) as it reduces the slowing-down time

of the energetic particles and therefore prevents the energetic tail to be strong enough for this difference to be significant regarding the neutron yield. Therefore, the main feature that makes a difference here are the thermal reactions, so a study on this is required in order to precisely explain the observed behaviour.

Thermal reactions are associated with the measured ion temperature T_i of the bulk plasma. In fact, looking at the time evolution of T_i in Fig. 4.1 it can be observed that during the neutron yield peak it is much higher in discharge 96947 than in 96482. One of the reasons for this may be the collisional heating caused by H minority during the ramp-up. In Fig. 4.6b it can be seen that the collisional power transferred from fast ICRH-driven ions to bulk ions in discharge 96947 is larger. This is so because of the good performance of moderate H minority concentrations ($\sim 4.5\%$) during the ramp-up phase, which effectively rises T_e and consequently the critical energy, and then boosts T_i via collisions.

4.3 ^{3}He heating in D plasmas

H minority is not the only heating scheme tested at JET. In fact, the approach of enhancing bulk ion heating and thermal reactions seems promising given the evidence in the previous section. That is why ^{3}He is also a good candidate to work as a minority population in D and D-T plasmas to perform ICRH. As it is much more massive than H, the critical energy will be also higher (see Eq. 2.18), so that the energy of the ^{3}He nuclei needs to be higher in order to transfer more power to electrons than to ions with Coulomb collisions. Actually, in the context of heating at the fundamental ^{3}He, the involved physics are quite different than in H minority heating. In this case D is no longer resonant at $\omega = \omega_{He}$ since $\omega_D = (4/3)\omega_{He}$. This relation also implies that as can be deduced from Eq. 2.16 the polarization of the fast wave will not be as good as in the H minority scheme. In order to study this scheme's performance, discharge 94671 (see Fig. 4.1) has also been modelled and compared with the previously studied discharge 96482 as they both have a minority concentration of $\sim 2.25\%$.

Taking into account all these features that ^{3}He offers to ICRH, the strategy to maximize the neutron yield in ^{3}He minority plasmas will consist of enhancing collisional heating so that thermal fusion reactions are boosted and therefore compensate the lack of non-thermal reactions with respect to the H scheme.

It is interesting to compare the RF power absorption of ^{3}He and H heating schemes, as they both work at the fundamental of the minority cyclotron frequency. Although for ^{3}He the wave polarization is worse, it appears that ^{3}He absorbs wave power as well as H, since in a single pass the wave is almost completely damped according to PION predictions. In Fig. 4.7a the RF absorbed power by each mechanism in the ^{3}He discharge 94671 and in the

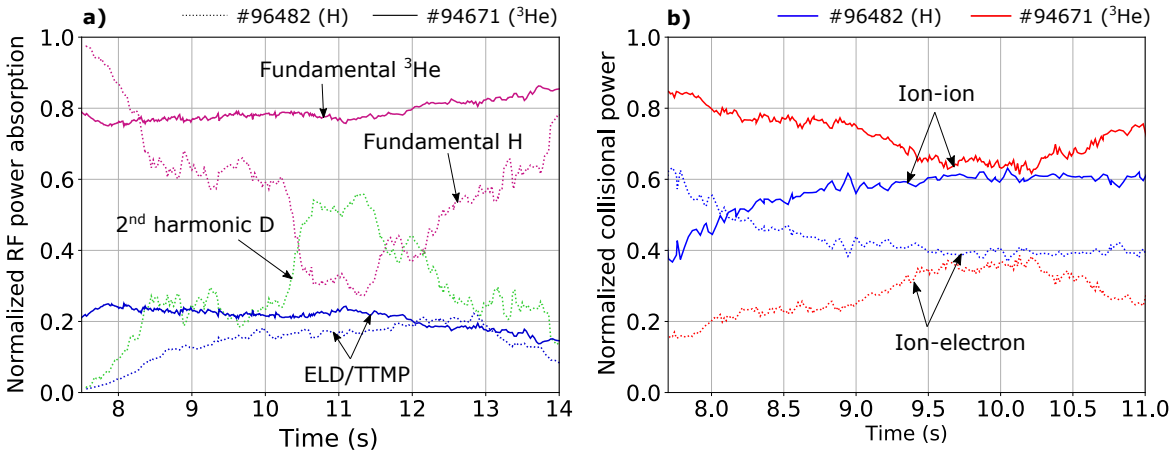

Fig. 4.7 *a) Normalized absorbed RF power by the resonant species (fundamental/purple and harmonic/green) and electrons (blue) for the ^{3}He minority discharge* 94671 *(solid) and the H minority discharge* 96482 *(dotted) for an input ICRF power of* ~ 5 *MW. b) Normalized collisional power transferred from ICRH-driven ions to background ions (solid) and to background electrons (dotted) of discharges* 96482 *(blue) and* 94671 *(red).*

H discharge 96482 is shown. One has to take into account that for the ^{3}He case only one damping mechanism of ion cyclotron harmonics is present, while in H minority two different mechanisms (fundamental H and 2nd D harmonic) compete. Regarding the direct electron damping via Landau damping and TTMP both schemes present approximately the same fraction of absorption $\sim 20\%$.

In order to boost thermal reactions, T_i must be significantly increased, so good bulk ion heating by Coulomb collisions must be achieved. That is why we analyse a ^{3}He minority discharge in the first place, as good performance is expected in this regard as compared with H. In Fig. 4.7b the comparison of the transferred collisional power in both discharges is shown, where a better performance on bulk ion heating is indeed observed in the ^{3}He minority case.

It is also observed that ion-electron collisions predominate during the ramp-up phase during discharge 96482 in contrast with discharge 94671. This is reasonable since during this phase, where T_e and n_e are lower, the critical energy is also lower and the only accelerated ions are the minority population in both cases. Nevertheless, this threshold is much higher for ^{3}He due to its higher mass. Therefore, the ICRH-driven ions in a ^{3}He heating scheme would have to surpass a much higher energy threshold than H to transfer more power to electrons, even if T_e is low.

Looking at the diagnostics in Fig. 4.1, nevertheless, it can be seen that discharge 94671 demonstrated poor performance regarding the neutron yield (65% lower than discharge 96482 with half of the plasma density). This is so because even T_i reaches similar or even

higher values than in H discharges, the enhanced number of thermal reactions is not able to compensate the lack of non-thermal reactions between resonant ions.

4.4 Chapter summary and discussion

The aim of this chapter was to simulate several plasma discharges that have been carried out at JET during the current D campaign and assess the involved physics with respect to plasma heating with the support of the theoretical background. In particular, two high performance discharges that used a H minority heating scheme and one discharge featuring ^{3}He minority were successfully modelled and studied in detail.

PION simulations allow us to assess the importance of heating mechanisms as the fusion reaction rate is highly nonlinear and difficult to predict. H minority concentrations of $\sim 4.5\%$ as in discharge 96947 show very good performance during the ramp-up, where the temperature is rapidly increased and the neutron rate soon reaches its peak. Therefore, bulk ion heating appears to play a crucial role in the neutron yield. Besides, by analysing the effect of H concentration in discharge 96947, it has been seen that fusion performance strongly depends on the wave power channeling to D ions. Lower H concentrations imply good D absorption during the main heating phase, which causes the development of an energetic tail in the distribution function and, thus, a boost in non-thermal reactions. In pure D plasmas this is specially important given that D-D fusion cross-section peaks at energies beyond the 2^{nd} harmonic absorption range. Actually, an increase of $\sim 30\%$ is expected in discharge 96947 for a $\sim 7\%$ difference in H concentration. Thus, puffing a minority population of H during the ramp-up and lowering its concentration during the main heating phase seems a promising way to achieve high performing discharges when using this scheme. This will not necessarily apply in D-T plasmas, which is discussed in Chapter 5.

^{3}He minority is then tested to assess whether its properties grant efficient bulk ion heating. Although collisional heating in this scheme appears to be better than in the H scheme, poor performance is demonstrated in low-density D plasmas, as D-D non-thermal reactions do not take place in this scenario. Even though collisional heating performs better than in H scenario, transferring more power to background ions in the same minority concentration conditions, it results insufficient to compensate the lack of non-thermal reactions. The viability of this scheme in D-T plasmas will be also discussed in Chapter 5.

Chapter 5

Extrapolation of a high performance discharge to a D-T scenario

5.1 Introduction

This chapter is an attempt to extrapolate a high performance plasma discharge to a different scenario where a 50%:50% D-T fuel is used with heating schemes based on minority populations of H and ^{3}He. These kind of extrapolations of present experiments are currently done at JET in preparation for the next D-T campaign (DTE2), which is programmed to begin in 2021[1]. During this campaign, JET is counting on many upgrades with respect to the previous (and only) D-T campaign DTE1 carried out in 1997, such as enhanced heating power, the ITER-like wall and new sets of diagnostics [12]. Therefore, it is of utmost relevance to assess if the tested plasma configurations that exhibited high performance in the present D majority campaign would offer similar properties in a D-T scenario.

The extrapolations are performed by taking one time slice of the original D discharge, changing the plasma conditions at this point and letting the system evolve under the new conditions until it reaches a steady-state solution. This is done using a stand-alone version of PION coupled to the PENCIL code, which computes the beam deposition. In this project the extrapolation of discharge 96482, which featured a longer high performance phase and $\sim 2\%$ H minority population, has been carried out.

To perform extrapolations to a 50%:50% D-T scenario, the initial conditions that have been given as input to PION are the following: half of the D of the original discharge is changed to T, both in the plasma composition and the NBI beams. The temperature and density profiles are obtained by fitting the following curve to the original profiles:

[1] https://www.euro-fusion.org/

$$f(s) = k + (1-k)\left(1-s^2\right)^a \tag{5.1}$$

Where s is the flux surface label and a and k the parameters to be fitted. This curve is re-normalized with the respective values of T_e and n_e at the center of the plasma at the time point where the extrapolation is performed. T_i is assumed to have the same form as T_e but multiplied by the temperature ratio factor T_i/T_e. The magnetic equilibrium of the original discharge is also given as initial condition. This is so because according to the Grad-Shafranov shift equation, the differences between a pure D plasma and a D-T scenario in that matter are predicted to barely affect the simulation results. The PENCIL code computes the beam source terms of both species, including T, for the Fokker-Planck equation also assuming a 50%:50% D-T plasma composition. The quasi-neutrality condition is kept in both codes.

In this new scenario the physics involved in the plasma heating are quite different from D plasmas. One of the main differences is the fact that the fusion cross-section of D-T reactions peaks at the keV range of energies and significantly falls for higher energies (see Fig. 1.1). As the D-T beams have energies of ~ 100 keV, a large number of fusion reactions will take place between beam-thermal ions. Therefore, ICRH enhancement is expected to be lower than in the D scenario. Fast ions above these optimal energies may be counterproductive for fusion performance and therefore a strong energetic tail in the distribution function is not desirable in this case [14].

5.2 H minority heating in a D-T scenario

The first heating scheme that is analyzed in the D-T scenario is heating at the fundamental H ($\omega = \omega_H$). To do so, the extrapolation on discharge 96482 has been performed at time $t = 12.34$s where the neutron rate production achieved its maximum. At this time point the temperature and density were $n_e = 0.9733 \cdot 10^{20}$ m^{-3}, $T_e = 6.825$ keV and $T_i/T_e = 1.3$. In this case T is also a resonant species, as $\omega = 3\omega_T$ (see Fig. 2.1). Following the same reasoning as for the D case, the new power partition between the three resonant species can be computed as done in [9]:

$$\frac{p_3}{p_1} = c_{31}\frac{m_3 k_\perp^4}{m_1 n_1 \omega_{c3}^4}\int v_3^4 f_3(v_3)dv, \tag{5.2a}$$

$$\frac{p_3}{p_2} = c_{32}\frac{m_3 k_\perp^2 \omega_{c2}^2}{\omega_{c3}^4 w_2}\int v_3^4 f_3(v_3)dv, \tag{5.2b}$$

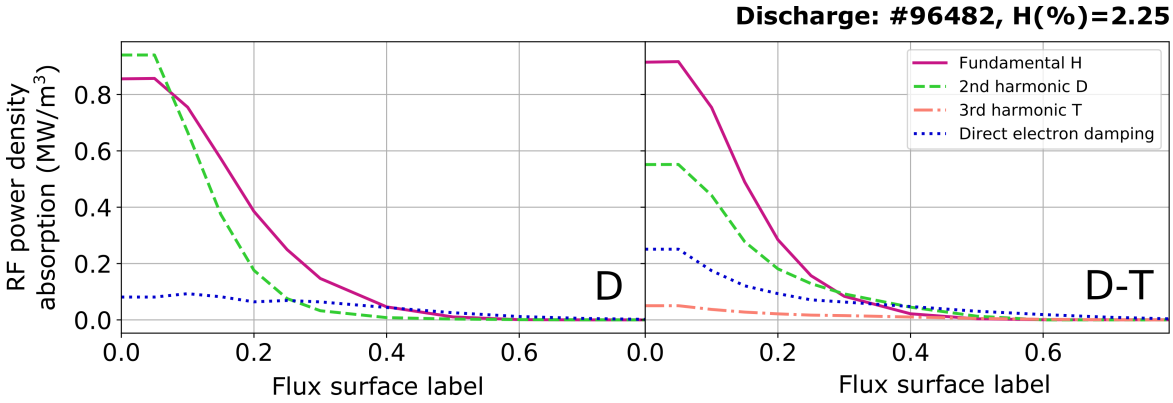

Fig. 5.1 *RF power absorption profiles of Fundamental H (solid), 2nd D harmonic (dashed), 3rd T harmonic (dash-dotted) and direct electron damping (dotted) of discharge* 96482 *for the D scenario (left) and 50%:50% D-T scenario (right) at the time of extrapolation ($t = 12.34$ s) and at the steady state respectively*

where the subscript 3 refers to T. The comparison of the RF power absorption profiles obtained in both scenarios is shown in Fig. 5.1. It can be seen that while H absorption remains almost equal than in the D scenario, 2$^{\text{nd}}$ D damping decreases significantly in this case. This is explained by an increase of the direct electron damping together with the lower D density, which has an impact in Eq. 4.1 by decreasing the D energy density term w_2. Besides, halving the D beams also contributes to make 2$^{\text{nd}}$ D absorption less effective. Actually, the volume integrated variables indicate that the drop in D power absorption in this scenario is $\sim 15\%$ with respect to the pure D plasma. The absorption profile of D, however, appears to broaden in D-T plasmas, which could be detrimental for bulk ion heating at the plasma center. Absorption by 3$^{\text{rd}}$ T harmonic happens to be very weak, so it hardly competes with the other absorption mechanisms. This is predicted by Eqs. 5.2a and 5.2b given the difference of two orders of magnitude lower than Eq. 4.1 for typical parameters of the studied scenarios [8].

Comparing the collisionallity in both scenarios (see Table 5.1 and Fig. 5.2) it can be seen that although the volume integrated collisional ion heating and collisional electron heating is very similar between the two scenarios, the profiles indicate that central heating is less effective in the D-T scenario. This can be explained by the broadened D absorption profile as seen previously. A decrease in central collisional heating could cause a drop on the central T_i and therefore be detrimental on the thermal reactions at the center, where the bulk of fusion reactions occur. In this regard, H minority scheme in D-T plasmas performs worse than in pure D plasmas.

	D	D-T
Ion-ion (MW)	20.94	20.88
Ion-electron (MW)	12.54	12.35
ELD/TTMP (MW)	1.00	1.28

Table 5.1 *Comparison of the volume integrated collisional ion heating, collisional electron heating and direct electron damping in the pure D and 50%:50% D-T scenarios, at* $t = 12.34s$ *and at the steady-state, respectively.*

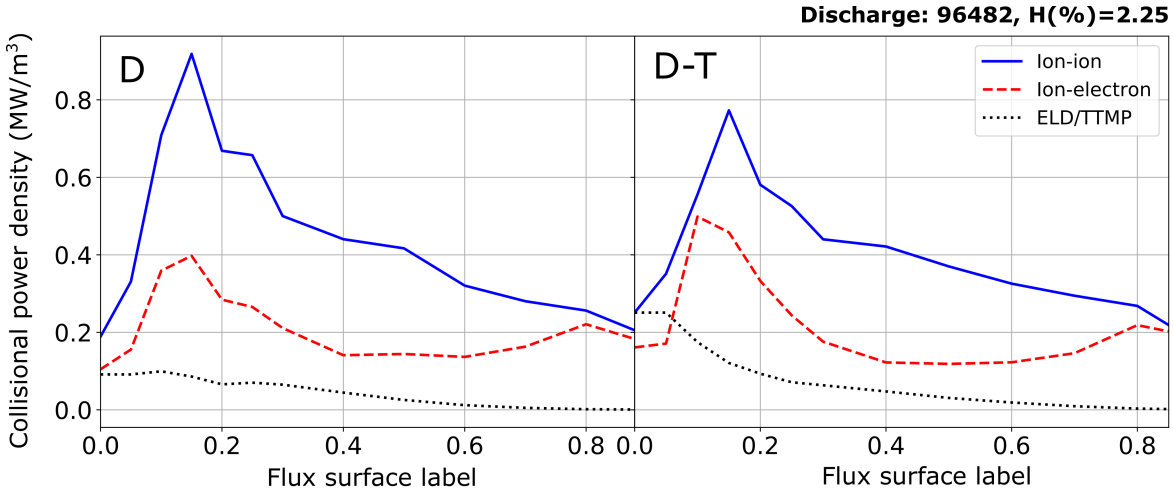

Fig. 5.2 *Collisional power density profiles and direct electron damping of discharge* 96482 *for the D scenario (left) and 50%:50% D-T scenario (right) at the time of extrapolation* ($t = 12.34$ *s) and at the steady state respectively*

5.3 Comparison of H and ^{3}He minority heating schemes in a D-T plasma

Performing an extrapolation of a high-performance discharge in a D-T plasma with a ^{3}He minority is specially interesting since this heating scheme will be eventually used at ITER. In this scheme, the same strategy is followed as in the D plasma scenario, that is to take profit of the high critical energy of the ^{3}He particles in order to effectively rise the ion temperature via ion-ion collisions and subsequently enhance the thermal fusion reactions. Nevertheless, in D-T plasmas T becomes also resonant at antenna frequencies and magnetic field tuned at the fundamental ^{3}He since $\omega_{He} = 2\omega_T$. This means that the 2$^{\text{nd}}$ T harmonic is expected to have a non-negligible contribution in the absorption of the fast wave and the power partition may be different.

Concentration (%)	**Minority density** (10^{19} m^{-3})		**D-T density** (10^{19} m^{-3})	
	H scheme	^{3}He scheme	H scheme	^{3}He scheme
0.0	0.0	0.0	4.332	4.418
2.0	0.173	0.173	4.245	4.245
4.0	0.347	0.340	4.158	4.078
6.0	0.520	0.500	4.072	3.918
8.0	0.693	0.654	3.985	3.764

Table 5.2 *Reference values of minority, D and T densities for the scan in concentrations. As the extrapolation is done from* $\sim 2\%$ *of minority concentration as in the original discharge, the values change accordingly.*

In this section the working background will be the same discharge studied in the H minority case, that is discharge 96482. It has been extrapolated to a ^{3}He minority scenario aiming to compare several heating features of both schemes. Notice that to provide a complete analysis of the ^{3}He minority scheme an integrated radial transport code would be needed to compute the corresponding T_i profile at the extrapolation point of discharge 96482, as we are assuming a temperature profile corresponding to a H minority discharge. Therefore, the neutron rate production is expected to be somewhat higher than the one that PION predicts. Nevertheless, this analysis is also interesting to assess the performance of both schemes under the same conditions. The reference temperature and density profiles are taken as in the H minority case as well as the magnetic equilibrium. The ICRH antenna frequency has been tuned to central fundamental ^{3}He resonance ($\omega = 33.2$ MHz, see Fig. 2.1) and the corresponding beam source terms have been computed with the beam code PENCIL. In this scenario D is not resonant and hence PION does not compute its contribution to the fusion yield. Therefore, the extrapolation to ^{3}He minority has been carried out assuming 15 MW of T-beam input power and 5 MW of ICRH. The contribution of the other 15 MW of D-beams to the fusion yield has been computed separately assuming 2$^{\text{nd}}$ D harmonic resonance frequency and NBI-only heating (i.e. no ICRH input power).

A scan in minority concentrations between $0-9\%$ has been performed by keeping the electronic density n_e constant throughout the scan, being the concentration defined as $n_m/(n_m+n_D+n_T)$, where n_m stands for the minority density (H or ^{3}He), and taking the concentration of $\sim 2\%$ from the original discharge as a reference. To perform the analysis of ^{3}He scheme, the ^{3}He density at 2% has been assumed to be the same as the H density in the H scheme. The same applies for D, T and the rest of the present elements in the plasma. Nevertheless, as ^{3}He has twice the electric charge of H, the n_e in the ^{3}He scheme has been

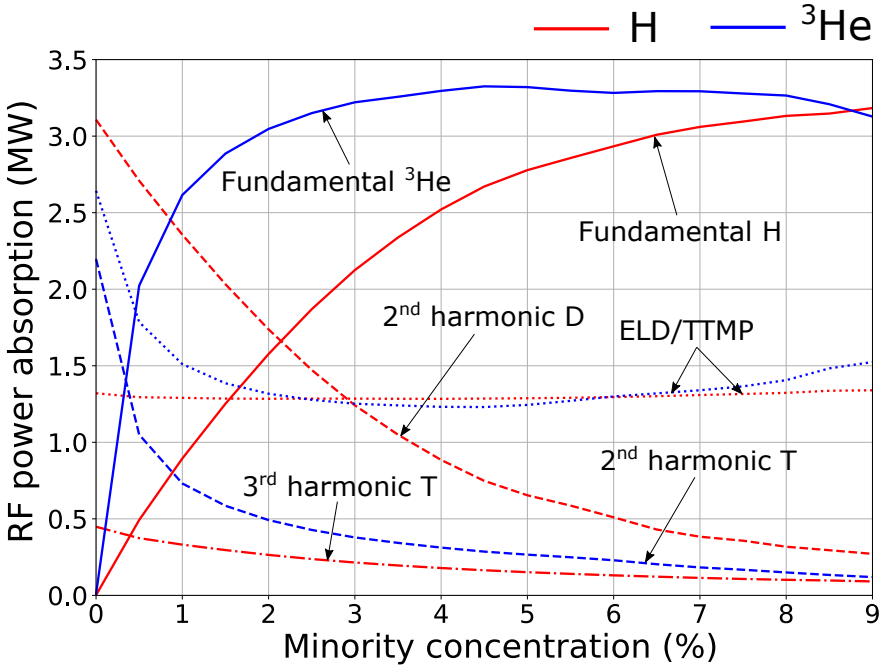

Fig. 5.3 *RF power absorption (Fundamental/solid, 2nd harmonic/dashed, 3rd harmonic/dash-dotted and direct electron damping/dotted) as a function of minority concentration (H in red and ^{3}He in blue) in discharge* 96482 *for an ICRH input power of 5MW in a D-T scenario.*

assumed a 1.78% higher in order to fulfill the quasi-neutrality condition. In Table 5.2 some reference values of the densities are shown.

5.3.1 RF absorption and collisional heating

As seen in Fig. 5.3, PION predicts strong absorption at the fundamental of ^{3}He while 2nd T harmonic remains more modest in comparison. In fact, fundamental ^{3}He absorption reaches its maximum at relatively low concentrations and is stabilized thereon. This is in contrast with the RF absorption in the H scheme, where fundamental H damping competes more tightly with 2nd D harmonic in a wider range of concentrations. As expected, 3rd T harmonic absorption in the H case is very weak in all the studied concentration range in comparison with other damping mechanisms. Direct electron damping also appears to play a significant role by absorbing 30% of the total wave power.

Regarding the collisional power transferred to thermal ions and electrons it is interesting to notice that the same behaviour as in the D plasma scheme is observed (see Fig.5.4), where the ICRH contribution of the transferred power is considered. This is computed by subtracting the collisional power in NBI-only simulations from the collisional power obtained with full heating (ICRH+NBI). The NBI contribution is found to be very similar in both schemes.

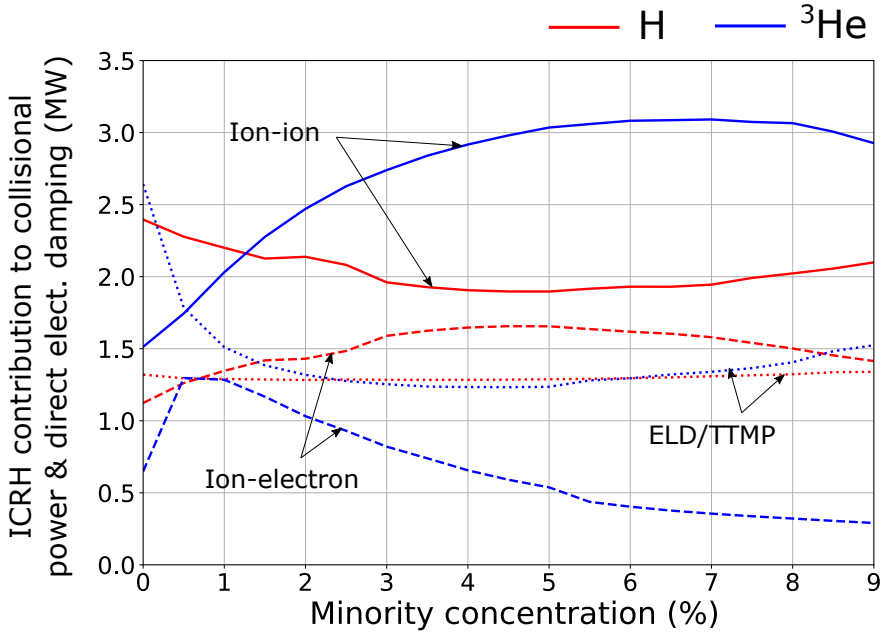

Fig. 5.4 *ICRH contribution to collisional power (to background ions/solid and to background electrons/dashed) and direct electron damping (dotted) as a function of minority concentration (H in red and ^{3}He in blue) in discharge* 96482 *for an ICRH input power of 5MW in a D-T scenario.*

Indeed, it is seen that ^{3}He is more efficient than H in bulk ion heating for concentrations above 1% where the minority absorption is stronger. In this range of concentrations the RF absorption of ^{3}He is dominant compared to harmonic absorption. Thanks to its high critical energy most of the absorbed power is transferred to background ions. This is confirmed as both curves follow the same tendency. H minority scheme appears to perform worse in this case, transferring only $\sim 40-50\%$ of the wave power to bulk ions.

5.3.2 Analysis of fusion performance in D-T plasmas

The resulting fusion power is also analyzed for a scan in minority concentrations as seen in Fig. 5.5a. It is worth noting that the same tendency is followed in both schemes, where the fusion power decreases as the minority concentration increases. In particular, in the NBI-only case, the fusion power is observed to decrease linearly. This effect is associated with the plasma dilution, as n_e is kept constant throughout the scan and hence, the higher is the concentration, the lower is the D-T density and less reactions may take place.

Regarding the power achieved with full heating (NBI+ICRH), it ranges from 9.7 to 12.2 MW in the H case and $8.5-12$ MW in the ^{3}He case. The performance of H minority scheme appears to be better than ^{3}He minority in all the studied concentration range. To complete

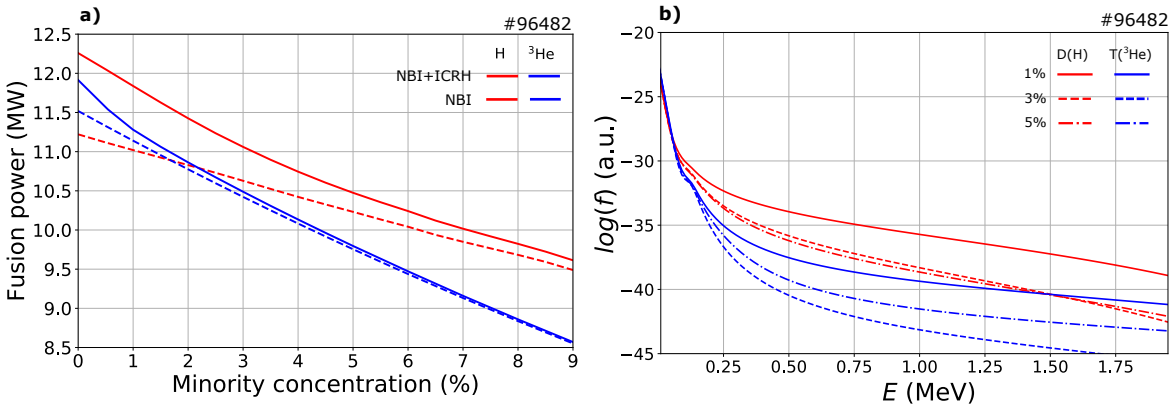

Fig. 5.5 *a) Fusion power achieved with full heating (solid) and NBI-only (dashed) as a function of minority concentration of H (red) and ^{3}He (blue) for discharge* 96482. *b) Distribution function at the plasma center at the steady-state of D (red) for the H minority scheme and T (blue) for the ^{3}He scheme for three different minority concentrations*

our analysis, nevertheless, an integrated radial heat transport code such as JETTO should be used to compute the proper T_i profiles and take into account the boost in thermal reactions that ^{3}He would provide. Regarding non-thermal reactions, The ICRF enhancement is higher in the H scheme, reaching a maximum value of $\sim 9\%$, while in the ^{3}He scheme, where the it reaches $\sim 3.5\%$. This is due to the high absorption of 2$^{\text{nd}}$ D harmonic in the H scheme as compared to the 2$^{\text{nd}}$ T harmonic in the ^{3}He scheme.

In Fig. 5.5b the distribution functions of D (in the H scheme) and T (in the ^{3}He scheme) at the steady state under full heating conditions are shown for different concentrations. In general, the tail strength of the T distribution function in the ^{3}He scheme appears to be weaker than the D tail in H. This is mainly explained by the poor 2$^{\text{nd}}$ T harmonic absorption as compared to 2$^{\text{nd}}$ D absorption. This also explains the lower ICRF fusion enhancement that ^{3}He presents as compared to H, since most of the reactions are thermal-thermal or beam-thermal and only few of them involve fast ICRH-driven ions. This does not appear to happen in any case, which means that in this plasma configuration even the most energetic particles are eventually slowed-down and undergo fusion so that the energetic tail does not continue to grow indefinitely and is kept controlled. This also explains why the ICRF enhancement in H scheme has similar values than in the pure D case, contrary to what we expected as explained in section 5.1. One explanation for this behaviour, apart from the high density of the plasma, is the worse RF absorption of D as compared to the pure D scenario. Therefore, the observed broadening of the absorption profile could in fact be beneficial for controlling the growth of an energetic tail in future experiments.

5.4 Chapter summary and discussion

This chapter was aiming to model ICRH in a D-T plasma using two different schemes in order to predict the heating performance of an studied plasma configuration for the next D-T campaign at JET.

Regarding the H minority scheme, in this scenario 3^{rd} T harmonic competes against the absorption mechanisms that appeared in pure D plasmas, although it seems that its role is verly limited. In D-T plasmas there is a decrease of $\sim 15\%$ in the 2^{nd} D harmonic absorption with respect to the pure D case, whose profile turns out to be more broadened as well than in the pure D scenario. Collisional heating in the H scheme appears to perform similarly as in D plasmas, although a detriment in central heating is observed, presumably as a consequence of this broadening of the absorption profile.

Some heating features have been compared between the H minority and the ^{3}He minority schemes by extrapolating the same discharge in a scan of minority concentration under the same density and temperature conditions. Strong correlation between the ^{3}He absorption and bulk ion heating has been observed in this scheme as a consequence of the high critical energy of ^{3}He. Besides, for moderate minority concentration values $\sim 5-7\%$, fast ions in the ^{3}He scheme appear to transfer $\sim 40\%$ more power to background ions than H scheme.

Regarding the distribution functions, a dependence of the tail strength with the minority concentration has been observed. In general, the T tail in ^{3}He has been found to be weaker than the D tail in H as a consequence of the poor T absorption. The tail formation does not seem to be detrimental to the fusion yield as the ion population in the D-T fusion optimal energy is still significant.

A fusion power of $9.5-12.5$ MW and $8.5-12$ MW using H and ^{3}He minority heating, respectively, is achieved. In this regard, the PION simulations that are shown in this chapter have been compared with codes such as JESTORR, which have been specially designed to compute the fusion power in D-T extrapolations. Excellent agreement has been found, being ~ 1 MW the maximum discrepancy with respect to PION results. As mentioned previously in this chapter, an analysis using an integrated radial transport code in the ^{3}He scheme would be interesting in order to predict more accurately the fusion yield. This would allow us to confirm if under such conditions ^{3}He would equal the results of H or perform even better. This D-T campaign, DTE2, unlike DTE1, will be carried out in the presence of the ITER-like-wall, which limits plasma operation [16]. The predicted results for DTE2, nevertheless, are similar as compared to the ones achieved in DTE1. Therefore, these predictions are considered to be satisfactory taking into account the difference in the circumstances regarding plasma operation between both campaigns.

Chapter 6

Conclusions and final remarks

This Final Degree thesis is focused on the modelling of several plasma discharges using the ICRH modelling code PION. PION allows to assess the heating physics at play in experiments that are carried out in tokamaks such as JET. Besides, it offers the possibility of testing new scenarios to help design future experiments. This is specially relevant in preparation for ITER plasmas, which are about to begin in the next few years.

In this project, in particular, plasma heating using ICRF waves in discharges with H and ^{3}He minority population has been studied in detail in different scenarios. The aim of this project was to validate the current models used in PION and assess the impact of ICRH to the neutron yield in D and D-T plasmas.

The validation has been carried out by modelling discharges 96482 and 96947 and comparing its predictions with experimental data. Excellent agreement has been found, which makes PION a useful tool to assess the physics regarding ICRH in such experiments. This analysis shows that in pure D plasma discharges featuring an H minority heating scheme, the channeling of the wave power to D ions is crucial for the neutron rate performance. Besides, H minority performs well during the ramp-up phase by increasing the temperature and enhancing thermal reactions in the studied plasma configurations. On the other hand, in D plasmas ^{3}He minority performance appears to be worse than H minority regarding the neutron rate production, although it provides interesting results concerning collisional heating.

An extrapolation of the high performing discharge 96482 to a 50%:50% D-T scenario has been carried out using a stand-alone version of PION and an integrated beam source code PENCIL. Performing such extrapolations is specially relevant in preparation for DTE2 and also for ITER plasmas as they will likely be fuelled with similar mixtures. According to our analysis the studied plasma configurations appear to perform well, achieving an equivalent fusion power of $9.5 - 12.25$ MW and $8.5 - 12$ MW in H minority and ^{3}He

minority, respectively. These results are considered satisfactory taking into account the results of the previous D-T campaign and the changes that JET has suffered ever since.

The results obtained in this project give an assistance to optimise fusion performance from the heating point of view in present discharges carried out at JET, and the extrapolations to different D-T scenarios performed in this work have contributed to the preparation of the forthcoming D-T campaign at JET, DTE2.

As a further work, as mentioned in chapter 5, a complete analysis of ^{3}He minority scheme using integrated radial transport codes is also appealing to assess its performance with proper temperature profiles. Other heating schemes such as the D minority are interesting to be studied as well, as they showed good performance in the previous D-T campaign at JET. Finally, more exotic schemes such as the three-ion scheme, which uses intrinsic beryllium impurities in the plasma, may be also explored as an alternative to the well-established minority schemes.

References

[1] Adams, J. et al. (1998). ICRF results in D-T plasmas in JET and TFTR and implications for ITER. *Plasma Physics and Controlled Fusion*, 40:A87–A103.

[2] Anderson, D., Eriksson, L. G., and Lisak, M. (1987). Anisotropic analysis of ion distributions distorted by ICRH in a tokamak plasma. *Plasma Physics and Controlled Fusion*, 29(7):891–900.

[3] Brunner, S. and Vaclavik, J. (1993). Dielectric tensor operator of hot plasmas in toroidal axisymmetrical systems. *Physics of Fluids B Plasma Physics*, 5:1695.

[4] Cohen, R. S. et al. (1950). The electrical conductivity of an ionized gas. *Phys. Rev.*, 80:230–238.

[5] Eriksson, L. G. and Helander, P. (1994). Monte Carlo operators for orbit-averaged Fokker-Planck equations. *Physics of Plasmas*, 1(2):308–314.

[6] Eriksson, L.-G. and Hellsten, T. (2006). A model for calculating ICRH power deposition and velocity distribution. *Physica Scripta*, 52:70.

[7] Freidberg, J. P. (2007). *Fusion power generation*, page 534–625. Cambridge University Press.

[8] Gallart, D. (2019). *Computational Analysis of Ion Cyclotron Resonance Frequency Heating for JET Experiments*. PhD thesis, ETSEIB, Universitat Politècnica de Catalunya.

[9] Gallart, D., Mantsinen, M., et al. (2018). Modelling of JET hybrid plasmas with emphasis on performance of combined ICRF and NBI heating. *Nuclear Fusion*, 58(10):106037.

[10] Gallart, D., Mantsinen, M., and Kazakov, Y. (2015). Modelling of ICRF heating in DEMO with special emphasis on bulk ion heating. volume 1689, page 060004.

[11] Garzotti, L. et al. (2019). Scenario development for D–T operation at JET. *Nuclear Fusion*, 59(7):076037.

[12] Joffrin, E. et al. (2019). Overview of the JET preparation for deuterium–tritium operation with the ITER like-wall. *Nuclear Fusion*, 59(11):112021.

[13] Llobet, X. et al. (1988). *in Theory in Fusion Plasmas*. Editrice Compositori, Bologna.

[14] Mantsinen, M. J. et al. (1999). Analysis of bulk ion heating with ICRH in JET high-performance plasmas. *Plasma Physics and Controlled Fusion*, 41(7):843–865.

[15] Mantsinen, M. J. et al. (2015). Bulk ion heating with ICRF waves in tokamaks. 1689.

[16] Matthews, G. F. et al. (2011). JET ITER-like wall—overview and experimental programme. *Physica Scripta*, T145:014001.

[17] Ongena, J. and Oost, G. (2012). Energy for future centuries - prospects for fusion power as a future energy source. *Transactions of Fusion Science and Technology*, 49:3–15.

[18] Rosenbluth, M. N. et al. (1957). Fokker-planck equation for an inverse-square force. *Phys. Rev.*, 107:1–6.

[19] Schnack, D. D. (2009). *Toroidal Equilibrium; The Grad–Shafranov Equation. In: Lectures in Magnetohydrodynamics. Lecture Notes in Physics*, volume 780. Springer, Berlin, Heidelberg.

[20] Start, D. et al. (1999). 39(3):321–336.

[21] Stix, T. H. (1972). Heating of toroidal plasmas by neutral injection. *Plasma Physics*, 14(4):367–384.

[22] Stix, T. H. (1992). *Waves in Plasmas*. New York.

[23] Swanson, D. G. (2003). Plasma waves (2nd edition). *Plasma Physics and Controlled Fusion*, 45(6):1069–1069.

[24] Wesson, J. (1973-1999). *The science of JET*. JET Joint Undertaking, Abingdon, Oxon.